Acta Pharmaceutica Sinica B 2025;15(5):2703−2722

Chinese Pharmaceutical Association
Institute of Materia Medica, Chinese Academy of Medical Sciences

Acta Pharmaceutica Sinica B

www.elsevier.com/locate/apsb
www.sciencedirect.com

ORIGINAL ARTICLE

A cisplatin prodrug-based self-assembling ozone delivery nanosystem sensitizes radiotherapy in triple-negative breast cancer

Tianyue Xu[a,†], Dan Zheng[a,b,†], Meixu Chen[a,†], Linlin Song[a,c], Zhihui Liu[a], Yan Cheng[b,d], Yujie Zhao[a], Liwen Huang[a], Yixuan Li[a], Zhankun Yang[e], Cong Li[g], Biao Dong[f,*], Jing Jing[a,*], Hubing Shi[a,*]

[a]*Institute of Breast Health Medicine, State Key Laboratory of Biotherapy, West China Hospital, Sichuan University and Collaborative Innovation Center, Chengdu 610041, China*
[b]*Cancer Center, Breast Center, West China Hospital, Sichuan University, Chengdu 610041, China*
[c]*Department of Ultrasound & Laboratory of Ultrasound Medicine, West China Hospital, Sichuan University, Chengdu 610041, China*
[d]*Multi-omics Laboratory of Breast Diseases, State Key Laboratory of Biotherapy, National Collaborative, Innovation Center for Biotherapy, West China Hospital, Sichuan University, Chengdu 610041, China*
[e]*College of Chemical Engineering, Shijiazhuang University, Shijiazhuang 050035, China*
[f]*National Clinical Research Center for Geriatrics and State Key Laboratory of Biotherapy, West China Hospital, Sichuan University, Chengdu 610041, China*
[g]*Core Facilities of West China Hospital, Sichuan University, Chengdu 610041, China*

Received 22 September 2024; received in revised form 28 December 2024; accepted 15 January 2025

KEY WORDS

Cisplatin;
Prodrug;
Radiotherapy;
Controlled-release system;
Ozone;

Abstract Lacking therapeutic targets highlights the crucial roles of chemotherapy and radiotherapy in the clinical management of triple-negative breast cancer (TNBC). To relieve the side effects of the chemoradiotherapy combination regimen, we design and develop a self-assembled micelle nanosystem consisting of perfluorocarbon chain-modified cisplatin prodrug. By incorporating perfluorodecalin, this nanosystem can effectively carry ozone and promote irradiation-derived reactive oxygen species (ROS) production. By leveraging the perfluorocarbon sidechain, the nanosystem exhibits efficient

*Corresponding authors.
E-mail addresses: biaodong@scu.edu.cn (Biao Dong), jingjing@wchscu.cn (Jing Jing), shihb@scu.edu.cn (Hubing Shi).
†These authors made equal contributions to this work.

Peer review under the responsibility of Chinese Pharmaceutical Association and Institute of Materia Medica, Chinese Academy of Medical Sciences.

https://doi.org/10.1016/j.apsb.2025.03.020

Triple-negative breast cancer;
Reactive oxygen species;
Immunogenic cell death

internalization by TNBC cells and effectively escapes from lysosomal entrapment. Under X-ray irradiation, ozone-generated ROS disrupts the intracellular redox balance, thereby facilitating the release of cisplatin in a reduction-responsive manner mediated by reduced glutathione. Moreover, oxygen derived from ozone decomposition enhances the efficacy of radiotherapy by alleviating tumor hypoxia. Notably, the combination of irradiation with ozone-loaded cisplatin prodrug nano system synergistically prompts antitumor efficacy and reduces cellular/systemic toxicity *in vitro* and *in vivo*. Furthermore, the combo regimen remodels the tumor microenvironment into an immune-favored state by triggering immunogenic cell death and relieving hypoxia, which provides a promising foundation for a combination regimen of immunotherapy. In conclusion, our nanosystem presents a novel strategy for integrating chemotherapy and radiotherapy to optimize the efficacy and safety of TNBC clinical treatment.

1. Introduction

The prognosis of breast cancer has markedly improved thanks to achievements in hormone therapy for hormonal receptor-positive subtypes and targeted therapy for HER2-positive subtypes using anti-human epidermal growth factor receptor 2 (anti-HER2) agents[1]. However, patients with triple-negative breast cancer (TNBC), which lacks these druggable targets, often rely on conventional treatments such as chemotherapy and radiotherapy. Chemotherapy holds significant importance in the systemic treatment of TNBC[2]. For example, cisplatin, one of the most commonly used chemotherapy drugs, disrupts DNA replication and eliminates rapidly dividing cells[3]. Based on the principle, the advantage of this chemotherapy is to clean the micronodules even if they are invisible. On the flip side, radiotherapy serves as a major local therapy approach for advanced breast cancer[4,5], particularly for patients who may not be suitable candidates for surgery. Radiotherapy exerts its antitumor effects primarily by directly causing DNA strand breaks and generating hydroxyl radicals, leading to the indirect killing of tumor cells. Therefore, the advantage of radiotherapy is to locally eliminate advanced tumors with a heavy burden.

The distinct antitumor mechanism and advantages of radiotherapy and chemotherapy provide a foundation for their combination in cancer treatment. Theoretically, the combination of irradiation and chemotherapy drugs, such as cisplatin, has a synergistic effect. This synergy can be attributed to two potential mechanisms referred to as "overlap" and "complementation"[6]. From the perspective of "overlap", platinum (Pt) in cisplatin boosts the generation of free radicals induced by ionizing radiation. Pt also captures free electrons liberated from irradiated DNA, causing chemical damage to DNA. From the perspective of "complementation", Pt not only induces tumor cell G2 arrest, amplifying the radiosensitivity of tumor cells, but also inhibits the repair of radiation-induced DNA damage. In turn, irradiation promotes the cellular uptake of Pt. In practice, combining local treatment (radiotherapy) and systemic therapy (chemotherapy) is beneficial to achieving more comprehensive efficacy. Radiotherapy effectively targets localized lesions, making it an ideal option for preventing local recurrence after surgery or treating a limited number of metastatic lesions to alleviate symptoms. Systemic chemotherapy can suppress or eradicate occult cancer cells, complementing the local treatment.

Inspired by these points, clinicians have combined chemotherapy and radiotherapy in controlling several malignant diseases, including head and neck cancer, larynx cancer, lung cancer, and stage II−III rectal tumors. For instance, in a clinical trial for patients with locally advanced larynx cancer, concomitant cisplatin/radiotherapy led to notable improvements in locoregional control and preservation of larynx compared with the induction cisplatin/fluorouracil arm or radiotherapy alone[7]. Furthermore, concurrent administration of chemotherapeutic drugs and irradiation has been found to be superior to sequential administration. In a Japan clinical oncology group study, concurrent chemoradiotherapy (etoposide and cisplatin) demonstrated better survival outcomes in the limited stage of small-cell lung cancer compared to sequential regimens, with a median survival time of 27.2 *vs*. 19.7 months[8]. Another clinical study on treating advanced laryngeal cancer with concurrent chemoradiotherapy reported that concurrent chemoradiotherapy with cisplatin is significantly superior to induction chemotherapy, followed by irradiation in terms of laryngeal preservation and locoregional control[9]. Additionally, clinical trials FFCD 92−03 and EORTC 22921 demonstrated that concurrent preoperative chemoradiotherapy remarkably improved the pathological complete response (pCR) as well as the local control rate of resectable rectal cancer[10].

However, in breast cancer, there is no distinction in terms of recurrence or survival outcomes between different sequencing formats of radiotherapy and chemotherapy. Concurrent chemoradiotherapy even increases the risk of side effects such as anemia, telangiectasia, and pigmentation[11]. Therefore, to apply concurrent chemoradiotherapy in TNBC and improve patient outcomes, some severe problems need to be addressed. Firstly, most chemotherapeutic agents have inevitable systemic toxicities, which are further exacerbated when combined with radiotherapy. Secondly, the hypoxic tumor microenvironment limits the efficacy of chemotherapy and radiotherapy. Thirdly, drug-induced cytotoxicity compromises (neutralizes or reverses) the T-cell-mediated tumor elimination that is promoted by immunogenic cell death (ICD) caused by the combination regimens.

To address these challenges, we design a self-assembled micelle nanosystem consisting of fluorocarbon chain-modified cisplatin prodrug. The nano micelle is loaded with perfluorodecalin (PFD) *via* its sidechain, which carries and delivers ozone into the tumor microenvironment. Upon internalization, the cisplatin prodrug in nano micelle backbone is transformed into cisplatin by the high level of reduced glutathione (GSH) present in tumor cells, a process further enhanced by ozone-derived reactive oxygen species (ROS) under irradiation stimulation. The released cisplatin, in combination with radiotherapy, synergistically

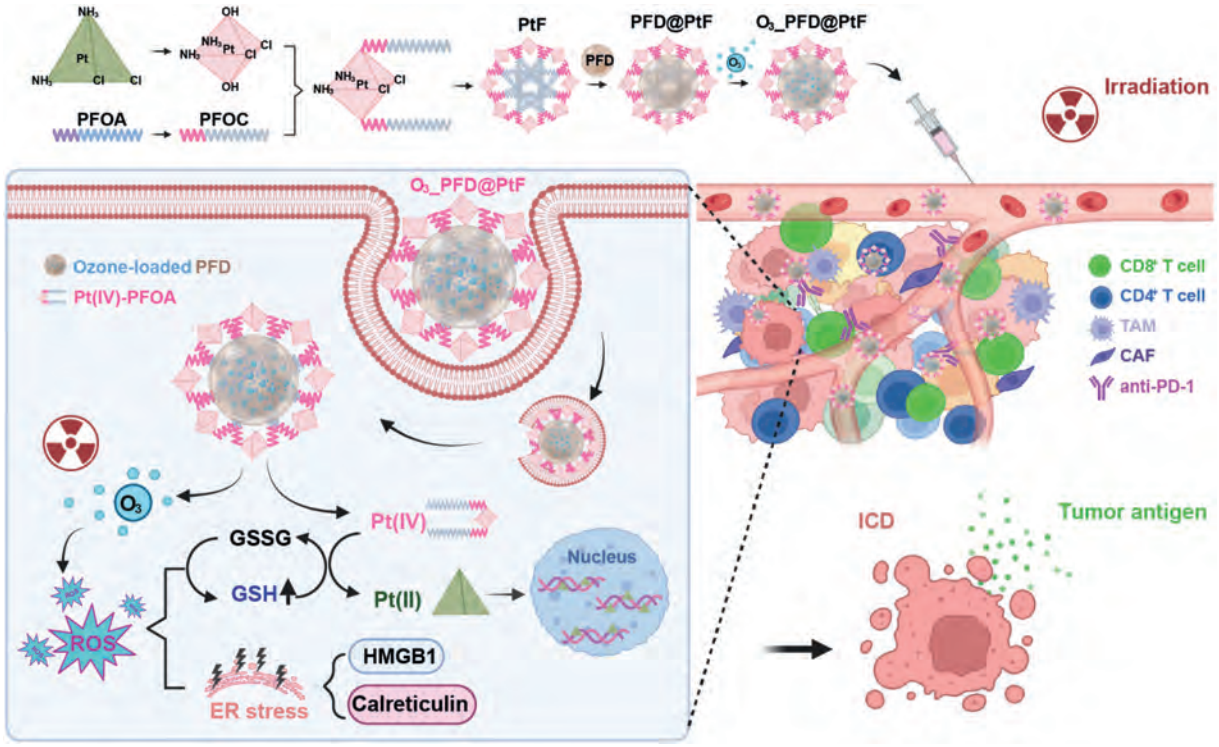

Figure 1 Schematic working model of O_3_PFD@PtF nanosystem. The platinum(IV) prodrug (Pt(IV)-PFOA), modified with perfluorocarbon chains, undergoes assembly with perfluorodecalin (PFD) to form PFD@PtF nanoparticles. Subsequently, the PFD@PtF particles are saturated with ozone (O_3). Following intravenous injection, the O_3_PFD@PtF particles accumulate within the tumor mass and are internalized by tumor cells. Under irradiation, the ozone generates reactive oxygen species (ROS) that facilitate the release of cisplatin (Pt (II)) from the platinum(IV) prodrug by influencing the ratio of reduced glutathione (GSH) and oxidized glutathione (GSSG) in the cytosol. Simultaneously, the ROS induces endoplasmic reticulum (ER) stress, calreticulin exposure, and high mobility group box 1 (HMGB1) release, which promote the tumor-specific neoantigen release by inducing immunogenic cell death (ICD). TAM, tumor-associated macrophage. CAF, cancer-associated fibroblasts (created with BioRender.com).

induces oncolysis (Fig. 1). The advantages of this nanosystem are: 1) the cisplatin prodrug specifically releases cisplatin within tumor cells, reducing systemic toxicity; 2) ozone decomposition under irradiation generates oxygen, improving the efficacy of radiotherapy by alleviating tumor microenvironmental hypoxia; 3) enhanced ICD and oxygen level create an immune-favorable microenvironment, laying the foundation for future combination with immunotherapy.

2. Materials and methods

2.1. Materials

Meryer Biochemical Technology Co., Ltd. (Shanghai, China) provided the cisplatin. PFD and perfluorooctanoic acid (PFOA) were acquired from J&K Scientific (Beijing, China). Macklin Biochemical Technology Co., Ltd. (Shanghai, China) supplied the thionyl chloride ($SOCl_2$). Thiazolyl blue tetrazolium bromide (MTT), terephthalic acid (TA), and bovine serum albumin (BSA) were acquired through Sigma−Aldrich (St. Louis, MO, USA). Fluorescein isothiocyanate (FITC) and NileRed fluorescence probe were obtained from MedChemExpress (Shanghai, China). Vitamin C sodium salt (NaVc) was provided by Aladdin Biochemical Technology Co., Ltd. (Shanghai, China). Tween-80 was acquired through BBI Life Sciences Corporation (Shanghai, China). Invitrogen (Carlsbad, CA, USA) supplied the Alexa Fluor 488 or Alexa Fluor 594-conjugated secondary antibodies and Alexa Fluor 647-conjugated wheat germ agglutinin (WGA). Beyotime Biotechnology Co., Ltd. (Nantong, China) provided the assay kit for GSH and oxidized glutathione (GSSG), citrate and ethylenediaminetetraacetic acid (EDTA) antigen retrieval solution, 2,7-dichlorodihydrofluorescein diacetate (DCFH-DA), and endogenous peroxidase-blocking buffer. Ozone was generated by ionizing oxygen with an ozone generator (Chuanghuan Ozone Electrical Equipment Co., Ltd., CH-ZTW3G, Guangzhou, China). Gibco Life Technologies (Grand Island, NY, USA) provided the fetal bovine serum (FBS), collagenase, deoxyribonuclease I (DNase I), and Hanks' balanced salt solution (HBSS). Merck Millipore (Billerica, MA, USA) provided streptomycin, penicillin, trypsin−EDTA, and radioimmunoprecipitation assay (RIPA). HyClone (Logan, UT, USA) provided the RPMI and DMEM medium. Secondary antibodies conjugated with species-specific horseradish peroxidase (HRP) and 3, 3′-diaminobenzidine (DAB) were acquired from Dako (Glostrup, Denmark).

2.2. Cells and mice

The SUM149 cell line was acquired from the State Key Laboratory of Biotherapy of Sichuan University (Chengdu, China). The 4T1, BT-549, and MCF-10A cell lines were acquired from the National Collection of Authenticated Cell Cultures (Shanghai,

China). The cells were all cultured in a completed RPMI/DMEM medium, which was supplemented with 10% FBS, 100 μg/mL streptomycin, and 100 U/mL penicillin in a 37 °C CO_2 incubator. The female BALB/c mice were obtained from Beijing HFK Bioscience Co., Ltd. (Beijing, China) and kept in specialized facilities under pathogen-free conditions. The mice received humane treatment throughout the experiments. The animal experiments followed the protocols approved by the Ethics Review Committee of Animal Experimentation of Sichuan University (20230302071, 20231221004).

2.3. Synthesis of Pt(IV)-PFOA

Cisplatin (100 mg) was suspended in distilled water (2.5 mL) at 55 °C under stirring. Then, 3.5 mL of hydrogen peroxide (H_2O_2) with a weight percentage of 30% was introduced into the mixture, which was then stirred at 55 °C for 1.5 h. Subsequently, the reaction solution was cooled to 4 °C overnight to allow complete crystallization of the resulting product, which was then collected by filtration. The collected precipitate was sequentially washed with pre-cooled distilled water (240 μL), absolute ethanol (240 μL), and absolute ether (600 μL) to obtain oxoplatin as a pale-yellow powder (yield: 80.5%).

To synthesize pentadecafluorooctanoyl chloride (PFOC), PFOA (1 g), $SOCl_2$ (104 μL), and *N*,*N*-dimethylformamide (DMF, 50 μL) were stirred and reacted under a nitrogen atmosphere at 75 °C for 4 h. After the reaction, the remaining $SOCl_2$ and DMF in the system were removed by rotary evaporation, yielding PFOC as a pale-yellow liquid (yield: 80.7%).

Subsequently, oxoplatin (100 mg) and excess PFOC were thoroughly mixed under nitrogen protection and reacted at 75 °C for 12 h. The product precipitate was washed with saturated sodium bicarbonate solution, followed by thorough washing with pure water. After drying the precipitate, a white powdery solid Pt(IV)-PFOA was obtained (yield: 31.4 %).

The products were dissolved in chloroform-*d* ($CDCl_3$) or dimethyl sulfoxide-d_6 (DMSO-d_6) and analyzed by ^{1}H-NMR and ^{9}F-NMR using a nuclear magnetic resonance (NMR) spectrometer (Bruker, Bruker Avance 400, Rheinstetten, Germany). Analysis of Fourier-transform infrared spectroscopy (FTIR, Bruker, INVENIO R, Ettlingen, Germany) was conducted. The molecule weight was measured by ultra-high-performance liquid chromatography coupled to high-resolution Orbitrap mass spectrometry (UHPLC−Orbitrap−MS, ThermoFisher Scientific, Q Exactive Plus, Bremen, Germany).

2.4. Preparation of micelle PtF and PFD@PtF

PtF nanoparticles were prepared by self-assembling Pt(IV)-PFOA using nanoprecipitation. A dimethyl sulfoxide (DMSO) solution of Pt(IV)-PFOA (100 μL, 15 mg/mL) was slowly added drop by drop into distilled water (2 mL) under 35 W ultrasound (Ningbo Scientz Biotechnology Co., Ltd., Ningbo, China) to facilitate the formation of PtF nanoparticles. After adding the organic phase, further ultrasonic treatment at 35 W (Ningbo Scientz Biotechnology Co., Ltd.) was applied to achieve a uniform particle size. The ultrasound (Ningbo Scientz Biotechnology Co., Ltd.) was programmed with a duty cycle of 5 s on and 2 s off, lasting for a total of 10 min. Finally, the resulting PtF nanoparticles were dialyzed with a 3500 D dialysis membrane to remove DMSO from the system.

To prepare the PFD@PtF, PFD (50 μL) was added to a Pt(IV)-PFOA acetone solution (1 mL, 2 mg/mL). The mixture underwent ultrasonication until emulsified. Afterward, the system received an additional 2 mL of distilled water, and sonication was maintained until a consistent emulsion was achieved. The dispersed PFD@PtF in water was obtained after removing the acetone in the system using rotary evaporation. To obtain O_3_PFD@PtF, we introduced ozone into the PFD@PtF by blowing for approximately 3 min until saturation was reached. The ozone gas was generated by ionizing oxygen, and the ozone concentration was 50 mg/L.

2.5. Characterization

The hydrodynamic diameter was determined using ZetaView TWIN PMX-220 (Particle Metrix, Meerbusch, Germany). Transmission electron microscope (TEM) images were captured using a JEOL microscope (JEOL, 1200 EX II, Tokyo, Japan).

The amount of Pt(IV)-PFOA loaded in the PFD@PtF was quantified by high-performance liquid chromatography (HPLC, Agilent Technologies, 1260 Infinity, Santa Clara, CA, USA) analysis as follows: After centrifuging the PFD@PtF, the resulting precipitates were dissolved in acetone until a concentration of approximately 1 mg/mL of Pt(IV)-PFOA was reached. Next, 5 μL of the organic solution was injected in a Sunfire Analysis C18 column (5 μm, 150 mm × 4.6 mm, Waters Corporation, Wexford, Ireland) and eluted with methanol and water in a ratio of 80:20. The signals were detected by an ultraviolet detector (Agilent Technologies) at 210 nm.

The drug loading (DL) of PFD was determined by quantifying PFD using gas chromatography (Agilent Technologies, 7890B, Wilmington, DE, USA). Specifically, the PFD@PtF nanoparticles were subjected to centrifugation (ThermoFisher Scientific, Sorvall Legend Micro 17R, Osterode am Harz, Germany) at 13,000 rpm for 10 min in order to break the emulsion and separate the loaded compound. Subsequently, the separated PFD was dissolved in 2 mL chloroform. The sample solution was injected into a gas chromatographic column (Agilent Technologies, DB-624, Santa Clara, CA, USA) using the headspace sampling method. The temperature of the column was initially set at 40 °C for 1 min. After that, it rose at a rate of 20 °C/min to a maximum temperature of 200 °C, which it maintained steadily for 5 min. The signals were detected using a flame ionization detector (Agilent Technologies). The calculation of the DL was performed as shown in Eq. (1):

$$\mathrm{DL}\,(\%) = W1/(W2 + W1) \times 100 \quad (1)$$

In this equation, *W*1 represents the weight of entrapped PFD, and *W*2 indicates the weight of entrapped Pt(IV)-PFOA.

2.6. Measurement of Pt release

Dynamic dialysis was performed to explore the release behavior of Pt from PtF nanoparticles in the presence or absence of NaVc. Specifically, PtF nanoparticles were separated in 1 mL of Tris-buffered saline (TBS) or 5 mmol/L NaVc solution (containing 0.75 mg/mL of Pt(IV)-PFOA). These particles were placed into a 3500 D dialysis bag and immersed in 20 mL corresponding solution, then shaken at 37 °C and 100 rpm (Shanghai Zhichu Instrument Co., Ltd., ZQTY-50S, Shanghai, China). At specific intervals, 2 mL of dialysate was sampled and substituted with an identical amount of the corresponding buffer solution. The

collected samples were digested overnight at 150 °C with concentrated nitric acid. Excess nitric acid was evaporated, and the remaining volume was diluted with dilute aqua regia. Platinum content was quantified using inductively coupled plasma mass spectrometry (ICP-MS, Agilent Technologies, Agilent 7900, Santa Clara, CA, USA).

2.7. Measurement of dissolved ozone

To assess the saturation of ozone, PFD@PtF nanoparticles, Tween-80 emulsified PFD (PFD-equivalent), and distilled water were saturated with ozone. Next, 1 mL of each sample was added to 2 mL of ozone-free distilled water. A pen-type detector (Clean Instruments Co., Ltd., CLEAN DOZ30, Xinbei, China) was used to monitor the change in ozone concentration in the ozone-free distilled water.

2.8. Hydroxyl radical generation of O_3_PFD@PtF

The generation of hydroxyl radicals was monitored using TA as a fluorescence probe. To accomplish this, distilled water, PtF, and PFD@PtF were either exposed to 20Gy X-ray irradiation (Rad Source Technologies, RS-2000, Buford, GA, USA) or not. Then, 50 mmol/L H_2O_2 and TA (1 mg/mL TA, 0.8 mg/mL NaOH) solutions were sequentially added to create a system that contained 12.5 mmol/L H_2O_2, 0.5 mg/mL TA, and 0.4 mg/mL NaOH. Fluorescent 2-hydroxyterephthalic acid resulting from the reaction between hydroxyl radical and TA can be identified using a fluorescence spectrophotometer (Bio-Tek Instruments, SYNERGY H1, Winooski, VT, USA) at approximately 435 nm when excited with light at 315 nm.

2.9. Cellular uptake of PtF

In an effort to evaluate the uptake of PtF in TNBC cells, both confocal laser-scanning microscopy (CLSM, Andor, Dragonfly 200, Belfast, UK) and flow cytometry (BD Biosciences, FACSAria III, San Jose, CA, USA) were utilized. TNBC cells were plated on glass slides in 12-well plates (5×10^4 per well) for CLSM (Andor) observation. Following an overnight period of incubation, cells were exposed to FITC-loaded PtF (30 μmol/L Pt(IV)-PFOA) for a duration of 0.5 h. For cell membrane visualization, the cells were stained with Alexa Fluor 647-conjugated WGA. Following 30 min fixation with 4% paraformaldehyde, the slides were prepared with an antifading 4′,6-diamidino-2-phenylindole (DAPI) mounting medium (YEASEN, Shanghai, China) and examined using CLSM (Andor). For flow cytometry (BD Biosciences) analysis, 5×10^5 cells were incubated in 6-well plates overnight. Medium containing NileRed-labeled PtF (30 μmol/L Pt(IV)-PFOA) was introduced and left to incubate for 0.5 h. After that, the cells were then washed, resuspended, and examined with flow cytometry (BD Biosciences) for uptake study.

To elucidate the internalization mechanism of PtF, classical internalization relevant biomarkers, including clathrin, caveolin-1, and lysosomal-associated membrane protein 1 (LAMP1), were visualized by immunofluorescence (IF). In brief, cell slides were treated with NileRed-labeled PtF (30 μmol/L Pt(IV)-PFOA) for 0.5 h. Following fixation with 4% paraformaldehyde for 20 min, the slides were treated with a 3% Triton X-100-10% BSA-PBS solution for 1 h at room temperature (RT). Subsequently, the cell slides were treated with primary antibodies targeting clathrin (Cell Signaling Technology, #4796S, Danvers, MA, USA), caveolin-1 (Cell Signaling Technology, #3267S), and LAMP1 (lysosome tracker, Abcam, ab208943, Cambridge, UK, mouse use; Cell Signaling Technology, #9091T, human use) at 4 °C overnight. Subsequently, the cell slides were treated with a secondary antibody labeled with Alexa Fluor 488 for 1 h at RT. The slides were prepared using an antifading DAPI mounting medium. High-magnification images were captured using CLSM (Andor).

2.10. Cytotoxicity measurement

The MTT assay was performed to evaluate cell viability. TNBC cells, normal mammalian epithelial cells, and immortalized lymphocytes were placed in 96-well plates (2000 per well). After 24 h, the cells were exposed to varying concentrations of PtF nanoparticles and cisplatin, respectively, with or without 20 Gy irradiation (Rad Source Technologies). TNBC cells were also exposed to varying concentrations of O_3_PFD@PtF particles with or without different doses of X-ray irradiation. After 96 h incubation, MTT solution was introduced (final concentration: 400 μg/mL). After incubating for an additional 4 h, the MTT-containing medium was substituted with 150 μL of DMSO, and the optical density (OD) at 570 nm was determined. The cell viability (%) was then calculated as shown in Eq. (2):

$$\text{Cell viability}\ (\%) = (\mathrm{OD_{test}} - \mathrm{OD_{blank}}) / (\mathrm{OD_{control}} - \mathrm{OD_{blank}}) \times 100 \quad (2)$$

GraphPad Prism software (GraphPad Software, 8.3.0, Boston, MA, USA) was used to determine the IC_{50} value at half-maximal inhibition.

2.11. Intracellular ROS and GSH/GSSG evaluation

The intracellular ROS generation was evaluated utilizing a DCFH-DA-dependent ROS assay kit. Firstly, TNBC cells were seeded onto cell slides in a 12-well cell culture plate (5×10^4 per well). After 24 h, TNBC cells were treated with serum-free DMEM cell−culture medium containing a diluted solution of DCFH-DA (1:1000 dilution) for 30 min. After PBS washing, cells were treated with PtF nanoparticles, O_3_PFD@PtF nanoparticles, and cisplatin individually for 2 h with or without 20 Gy irradiation (Rad Source Technologies). After being rinsed, the slides were mounted with DAPI medium. Images were captured using CLSM (Andor).

In order to examine the levels of GSH and GSSG in cells, 2×10^5 TNBC cells were incubated in 6-well plates for 24 h. The cells were exposed to PtF nanoparticles, O_3_PFD@PtF nanoparticles, and cisplatin at a concentration equivalent to 5 μmol/L of cisplatin, along with ozone-loaded perfluorodecalin emulsion, either with or without irradiation. After 24 h incubation, the GSH and GSSG levels in cells were determined using GSH and GSSG assay kits.

2.12. Intracellular Pt/DNA measurement

In order to detect cisplatin release *in vitro*, the Pt content in the nucleus DNA was measured. TNBC cells were placed into 6-well plates (2×10^5 per well). After 24 h, the cells were then exposed to PtF nanoparticles, O_3_PFD@PtF nanoparticles, and cisplatin at a concentration equivalent to 5 μmol/L of cisplatin, with or

without 20 Gy irradiation (Rad Source Technologies). Following 24 h incubation, the cells were collected. To measure Pt/DNA, the nucleus DNA was extracted utilizing the phenol/chloroform extraction method and quantitatively determined using a spectrophotometer (ThermoFisher Scientific, NanoDrop One, Waltham, MA, USA). Subsequently, concentrated nitric acid was used to digest the cell DNA, and then ICP-MS (Agilent Technologies) was applied to perform Pt content analysis.

2.13. Western blot

In order to conduct the western blot analysis, SUM149 cells were plated in 6-well plates (5×10^5 per well) and allowed to incubate for 24 h. Subsequently, the cells were exposed to PtF nanoparticles, O_3_PFD@PtF nanoparticles, and cisplatin at a concentration of 10 μmol/L, with or without 20 Gy irradiation (Rad Source Technologies). After 24 h, cells were disrupted with RIPA solution containing phosphatase and protease inhibitors. Protein samples were electrophoresed and then moved onto polyvinylidene fluoride membranes (Merck Millipore, Carrigtwohill, Ireland). Following that, western blots analysis was conducted with antibodies for calreticulin (CRT, Abcam, ab92516), high mobility group box 1 (HMGB1, Abcam, ab79823), and β-ACTIN (ASGB-Bio, TA-09, Beijing, China).

2.14. Study of biodistribution and therapeutics in tumor-bearing mice

For the biodistribution study and therapeutic evaluation, female BALB/c mice (7 weeks, 18−20 g) were used to establish the TNBC tumor model. To establish the subcutaneous tumor model, 5×10^5 4T1 or luciferase-expressing 4T1 (4T1-Luc) cells were injected subcutaneously on the right or both dorsal flanks of each mouse. For the lung metastatic tumor model, each mouse was injected 2×10^5 4T1-Luc cells through the tail vein.

For biodistribution analysis of PtF, NileRed-labeled PtF nanoparticles were injected into the mice intravenously once the tumor size reached around 200 mm^3. At the specified time points (1, 6, 12, and 24 h) post-injection, the mice were humanely euthanized. Tumors and major organs (including the heart, liver, spleen, lung, and kidney) were collected and analyzed with fluorescence imaging (excitation: 500 nm, emission: 600 nm) utilizing the small animal fluorescence imaging system (PerkinElmer, IVIS Spectrum, Waltham, MA, USA).

The therapeutic efficacy of O_3_PFD@PtF under X-ray irradiation was evaluated in mice bearing subcutaneous 4T1 tumors. Upon the subcutaneous tumor volume reaching approximately 100 mm^3, the mice were randomly divided into various treatment groups ($n = 6$): (1) PBS (Blank), (2) PtF, (3) cisplatin, (4) O_3_PFD@PtF, (5) PBS plus X-ray irradiation, (6) PtF plus X-ray irradiation, (7) cisplatin plus X-ray irradiation, and (8) O_3_PFD@PtF plus X-ray irradiation. Each reagent was administered intravenously every 3 days at a cisplatin-equivalent dose of 0.8 mg/kg of body weight. The injection was administered 3 times with or without localized X-ray irradiation (6 Gy/fraction, Rad Source Technologies) on the right dorsal flank 6 h after injection. Tumor diameters were assessed with a vernier caliper every 3 days before treatment and every other day after treatment. The tumor volume was computed as shown in Eq. (3):

$$\text{Tumor volume} = (\text{Tumor length}) \times (\text{Tumor width})^2/2 \quad (3)$$

Additionally, the mice's body weight was recorded every 2 days following the treatment. The mice were euthanized on Day 26 after tumor injection, and both the tumors and major organs were excised.

In the 4T1 lung metastatic mice model, the antitumor efficacy of O_3_PFD@PtF combined with X-ray irradiation was also examined. On Day 6 post-inoculation, the mice were assigned to various treatment groups ($n = 6$), as mentioned above. Each reagent was administered intravenously at a cisplatin-equivalent dosage of 0.8 mg/kg body weight every 2 days. This injection was repeated 3 times in the presence or in the absence of whole-body X-ray irradiation (2 Gy/fraction, Rad Source Technologies) at 6 h after injection. The growth of lung metastatic tumors was measured using bioluminescence imaging (Spectral Instruments Imaging, KINO, Tucson, AZ, USA) starting from Day 5 after inoculation and then every 2 days. On Day 13 post-inoculation, the mice were euthanized in a human manner, and their lungs were dissected for additional analysis.

2.15. Immunohistochemistry and immunofluorescence staining

The samples of tumors and major organs were fixed using a solution of 10% formalin, followed by embedding in paraffin and cutting into 4 μm-thick slides. These slides were then placed onto glass slides and subjected to staining with hematoxylin−eosin (H&E). For immunohistochemical (IHC) and IF staining, the obtained tumor sections were first deparaffinized and then exposed to 3% H_2O_2. Antigen retrieval was carried out by subjecting the samples to microwave irradiation at 95 °C for 16 min using either EDTA (pH = 9.0) or citrate (pH = 6.0) buffer.

For IHC, the tumor slides were sequentially treated with an endogenous peroxidase-blocking buffer in the dark for 15 min and 5 % BSA for 1 h at RT. Following a rinse with PBS, the slides were incubated overnight at 4 °C with primary antibodies including BAX (Cell Signaling Technology, #14796), Cleaved caspase-3 (Cell Signaling Technology, #9664), Ki67 (Cell Signaling Technology, #12202), CRT (Abcam, ab92516), HMGB1 (Abcam, ab79823), and heat shock protein70 (HSP70, Abcam, ab194360). Afterward, the tumor samples were washed with PBS and exposed to secondary antibodies conjugated with species-specific HRP at RT for 40 min. After another round of PBS washing, the slides were visualized using DAB. The slides were subsequently processed by water washing, hematoxylin counterstaining, ethanol dehydrating, and media mounting.

For IF staining, the tumor slides were incubated with 5 % BSA at RT for 1 h, followed by a PBS rinse. Following this, the slides underwent treatment with either CD4 antibody (Abcam, ab183685) or CD8α antibody (Abcam, ab217344) for an overnight incubation at 4 °C. After two PBS rinses, the slides were exposed to Alexa Fluor 488 or Alexa Fluor 594-conjugated secondary antibodies in 5% BSA at 37 °C for 40 min. Finally, the slides were mounted using an antifading DAPI mounting medium for fluorescence imaging.

2.16. Flow cytometry analysis

In order to assess the tumor-infiltrating lymphocyte of each treatment group, single-cell suspensions were prepared following the method below: tumor samples were dissected into small pieces using scissors in MACS Tissue Storage Solution (Miltenyi Biotec, Bergisch Gladbach, Germany). Tissue pieces were broken down

using a combination of collagenase type I and type IV (1 mg/mL) along with DNase I (50 μg/mL) at 37 °C for a duration of 10 min. Then, digested tissues were passed through a cell strainer to obtain single-cell suspensions. After rinsing the suspensions twice with the HBSS buffer, they were subsequently resuspended in the same HBSS buffer.

Different fluorophore-conjugated anti-mouse antibodies were used to co-stain the cells: CD45-APC-Cyanine7 (BioLegend, 103116, San Diego, CA, USA), CD3-PE (BioLegend, 100205), CD4-FITC (BioLegend, 100510) and CD8-Brilliant Violet 510 (BioLegend, 100752). Multiparameter staining was used to differentiate the specific cell groups: tumor-infiltrating $CD3^+$ T-cells ($CD45^+CD3^+$), tumor-infiltrating $CD8^+$ T-cells ($CD45^+CD3^+CD8^+$), and tumor-infiltrating $CD4^+$ T-cells ($CD45^+CD3^+CD4^+$). Following the staining process, flow cytometry (BD Biosciences) was used to analyze the cells, and FlowJo_v10.6.2 software (BD Biosciences, San Jose, CA, USA) was utilized to process the data. Nonviable cells and doublets were eliminated using forward and side scatter characteristics.

2.17. *Statistical analysis*

GraphPad Prism 8 (8.3.0) was utilized for the statistical analysis. The results were presented in the form of mean ± standard deviation (SD). Two-way ANOVA analysis was performed for

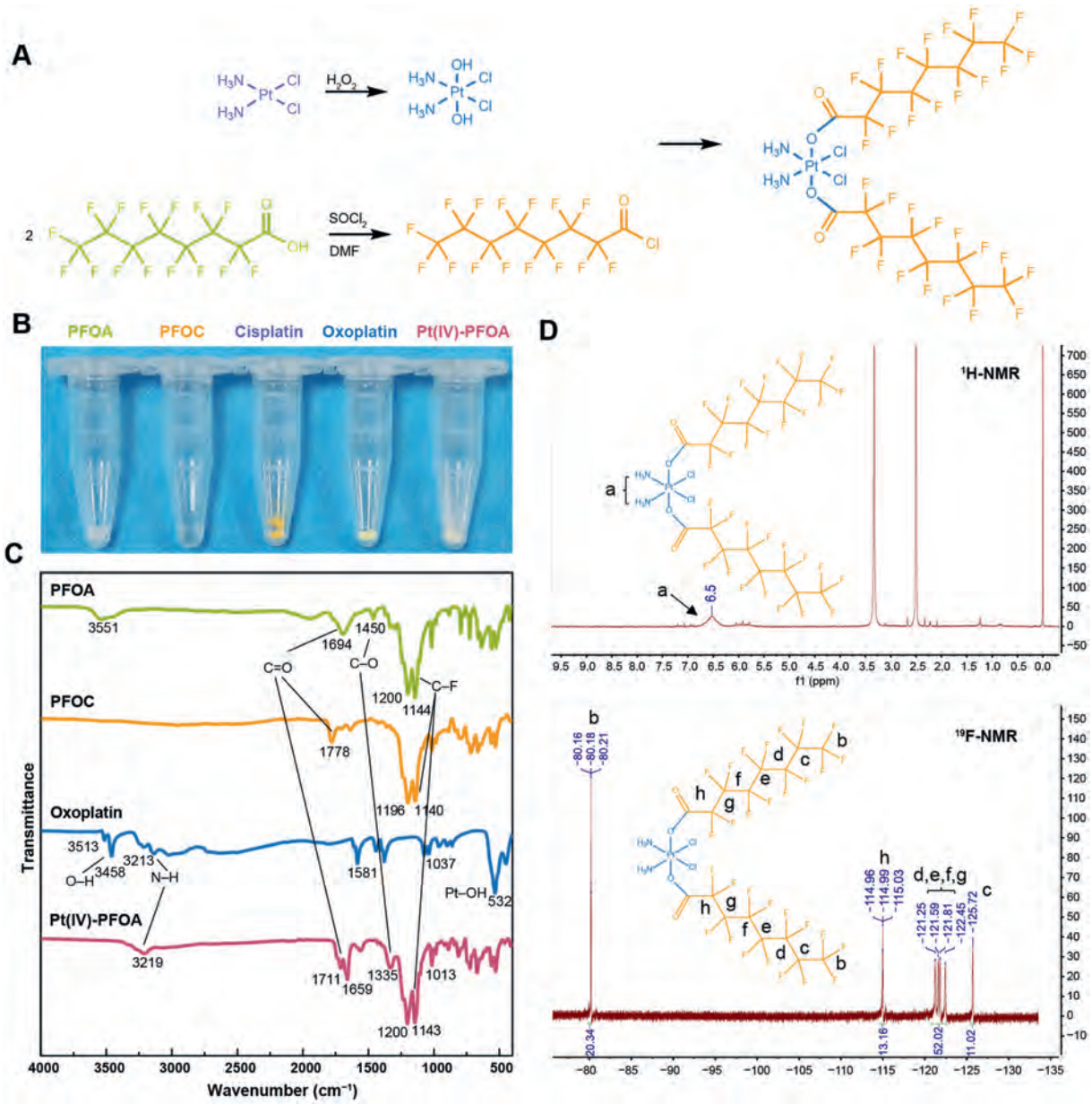

Figure 2 The synthesis of cisplatin prodrug Pt(IV)-PFOA. (A) Chemical structure and synthetic route of Pt(IV)-PFOA. H_2O_2, hydrogen peroxide. $SOCl_2$, thionyl chloride. DMF, *N*, *N*-dimethylformamide. (B) The appearance of perfluorooctanoic acid (PFOA), pentadecafluorooctanoyl chloride (PFOC), Cisplatin, Oxoplatin, and Pt(IV)-PFOA. (C) Fourier-transform infrared spectrophotometer (FTIR) spectra of PFOA, PFOC, Oxoplatin, and Pt(IV)-PFOA. (D) ^{1}H-NMR spectrum and ^{19}F-NMR spectrum of the final product Pt(IV)-PFOA.

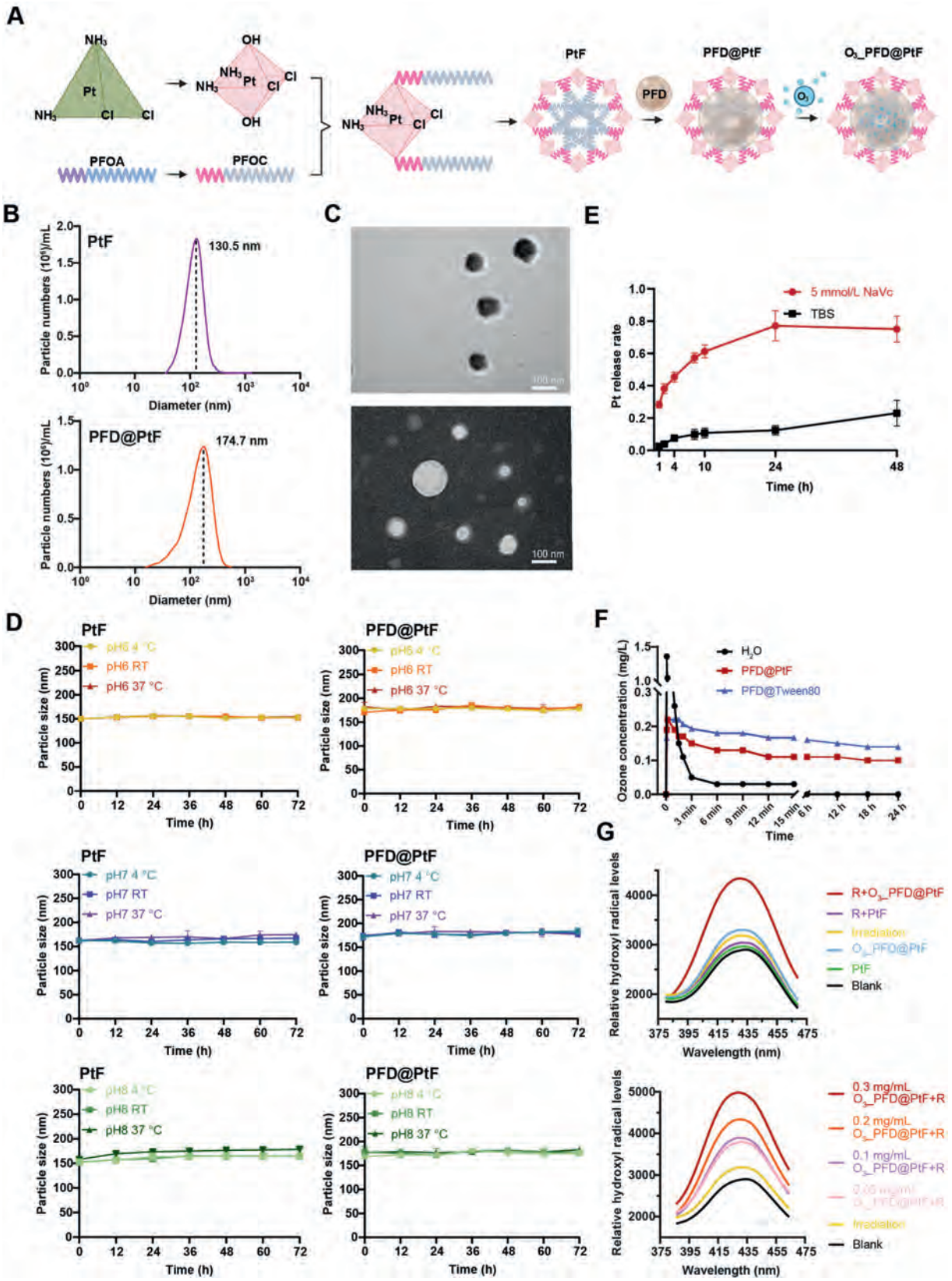

Figure 3 Construction procedure and characterization of PtF and PFD@PtF micelles. (A) The preparation process of PtF, PFD@PtF, and O_3_PFD@PtF (Created with BioRender.com). PFOA, perfluorooctanoic acid. PFOC, pentadecafluorooctanoyl chloride. PFD, perfluorodecalin. O_3, ozone. (B) Hydrated diameter distribution of PtF and PFD@PtF. (C) PtF visualized by Transmission electron microscope (TEM). Scale bar = 100 nm. (D) The particle size of PtF and PFD@PtF at 4 °C, RT, and 37 °C in indicated pH values. Data are shown as mean ± SD (n = 3). RT, room temperature. (E) Release curves of platinum (Pt) from PtF in 5 mmol/L Vitamin C sodium salt (NaVc) and Tris-buffered saline (TBS).

multiple comparisons in Figs. 4D−M, 5A, D, F, 6G, H, 7E−G, 8E, 9D−F, I, J, L, M and Supporting Information Figs. S8B and S8C. The statistical parameters, encompassing the *F* and *P* values for factors and interaction, were included in the Supporting Information Table S1−S13.

3. Results

3.1. Synthesis of cisplatin prodrug Pt(IV)-PFOA

To constitute the self-assemble small-molecule prodrug nanoparticles, a platinum(IV) prodrug (Pt(IV)-PFOA) tethering with two PFOA molecules is synthesized according to the route illustrated in Fig. 2A. Firstly, oxoplatin is obtained by oxidization of cisplatin with H_2O_2. Secondly, PFOC is synthesized by an acylating chlorination reaction with PFOA and $SOCl_2$. Finally, the Pt(IV)-PFOA is obtained by esterification between PFOC and oxoplatin, as indicated in Fig. 2A. The appearance of the final product Pt(IV)-PFOA, raw compound, and intermediate products are shown in Fig. 2B.

The structure of Pt(IV)-PFOA and the synthesis process are quality controlled by FTIR, ^{1}H-NMR, and ^{19}F-NMR (Fig. 2C and D; Supporting Information Figs. S1 and S2). The FTIR spectrum of oxoplatin exhibits the stretching vibration peaks of −OH and Pt−OH at 3458 and 532 cm^{-1}, respectively, indicating the correct synthesis of oxoplatin. Comparing the FTIR spectra of PFOC and PFOA, it is observed that the −OH stretching vibration peak at 3551 cm^{-1} and the C−O stretching vibration peak at 1450 cm^{-1} disappears, proving the production of PFOC. Meanwhile, the stretching vibration peak of C═O is red-shifted from 1694 to 1778 cm^{-1}, which confirms the proper transformation of acyl chloride from carboxylic acid. In the FTIR spectrum of Pt(IV)-PFOA, the C═O stretching vibration peak at 1711 cm^{-1} and the C−O stretching vibration peak at 1335 cm^{-1} indicate the formation of the ester bond. The peaks of C−F stretching vibration at 1200 and 1143 cm^{-1} are attributed to fluoroalkyl groups derived from PFOA. In addition, no peak between 3300 and 3600 cm^{-1} is observed, suggesting the absence of the −OH group. It indicates that both hydroxyl groups in oxoplatin have reacted with PFOC and PFOA in synthesized Pt(IV)-PFOA are covalently connected as axial ligands.

In the ^{1}H-NMR spectrum of Pt(IV)-PFOA, the amino H appearing at 6.5 ppm (a) is attributed to the ammonia ligands of platinum(IV). In the ^{19}F-NMR spectra, the peaks that appeared at −80.18 ppm (b, $-CF_3$),−125.72 ppm (c, $-CF_2-CF_3$), −121.25 to −122.45 ppm (d, e, f, g, $-CF_2-$), and −114.99 ppm (h, $-O-CO-CF_2-$) confirmed the presence of fluoroalkyl groups in Pt(IV)-PFOA. In summary, the successful synthesis of Pt(IV)-PFOA is confirmed by analyzing the results obtained from FTIR, ^{1}H-NMR, and ^{19}F-NMR.

Furthermore, the molecular weight of Pt(IV)-PFOA is determined by UHPLC-Orbitrap-MS analysis (Supporting Information Fig. S3). In the mass spectrum of Pt(IV)-PFOA, the exact molecular ion mass of $[M + H]^+$, $[M + NH_4]^+$ and $[M + Na]^+$ are observed at *m/z* 1125.89, 1142.92, and 1147.87, respectively, which are in excellent agreement with the corresponding theoretical simulation results simulated by Thermo Xcalibur Qual Browser software (ThermoFisher Scientific, version 4.3, Waltham, MA, USA). These data pinpoint the molecular weight of Pt(IV)-PFOA to be 1126.17 g/mol.

3.2. Preparation and characterization of micelle PtF and PFD@PtF

The synthesized prodrug Pt(IV)-PFOA can form nano-scaled particles either alone (PtF) or with PFD (PFD@PtF) through self-assembly based on the hydrophobic interaction between fluorine residues (Fig. 3A). The self-assembled PtF nanoparticles are prepared using the nanoprecipitation method by adding a DMSO solution of Pt(IV)-PFOA dropwise into an aqueous solution under ultrasound. The PtF particle presents uniform spherical morphology revealed by TEM (Fig. 3C) with a hydrated diameter of around 130 nm (Fig. 3B). To efficiently load ozone, PFD, an excellent ozone solvent, is incorporated into PtF nanoparticles based on the similarity-intermiscibility theory, resulting in PFD@PtF nanoparticles with a hydrated diameter of around 170 nm (Fig. 3B). Our results demonstrate a high maximal incorporation rate of 91.24% (PFD/PFD@PtF), ensuring effective ozone loading and delivery. To evaluate the stability of PtF and PFD@PtF nanoparticles, we measure their hydrated diameter at indicated temperatures and pH values. The results indicate that both PtF and PFD@PtF particles remain stable for up to 72 h under acidic, alkaline, and neutral conditions at 4 °C, RT, and even 37 °C, respectively. This excellent stability fulfills the criteria for *in vitro* as well as *in vivo* uses (Fig. 3D).

According to our design strategy, cisplatin can be released from the Pt(IV)-PFOA prodrug in a reductive environment, such as the cytosol of tumor cells. In order to verify this, PtF nanoparticles are incubated with a buffer containing NaVc at 37 °C. ICP-MS results demonstrate that the reductive environment remarkably promotes the release of cisplatin and the disintegration of PtF nanoparticles. After 24 h incubation in 5 mmol/L NaVc, as much as 77.0% of cisplatin is released from PtF particles (Fig. 3E). The strong electron-withdrawing effect by fluorine atoms facilitates the reduction of platinum(IV) to platinum(II) and consequently boosts the release of cisplatin.

To measure the ozone loading capacity of PFD@PtF particles, ozone release curves are profiled with ozone-saturated water solution (negative control), Tween-80 emulsified PFD (positive control), and PFD@PtF particles (Fig. 3F). The results reveal that the ozone loading capacity of PFD@PtF vehicles is approximately 20-fold higher than that of water solution. Furthermore, the release curves indicate that PFD@PtF nanoparticles exhibit a slow and sustained ozone-releasing capacity for up to 24 h. Upon X-ray irradiation, the ozone-loaded particles decompose into ROS and oxygen, providing a foundation for improving radiotherapy. The results of the TA assay show that ozone-loaded PFD@PtF particles (O_3_PFD@PtF) efficiently generate ROS under X-ray ionizing conditions (Fig. 3G). The amount of ROS is positively correlated with the amount of O_3_PFD@PtF.

3.3. Biodistribution and cytotoxicity of PtF and PFD@PtF in vitro

We investigate the subcellular distribution of FITC-labeled PtF nanoparticles in three TNBC cell lines, including one murine (4T1)

Data are exhibited as mean ± SD ($n = 3$). (F) The dynamic release curve of ozone carried by PFD@PtF and PFD@Tween80. (G) Hydroxyl radical productivity of O_3_PFD@PtF in the presence or in the absence of irradiation assessed by terephthalic acid assay.

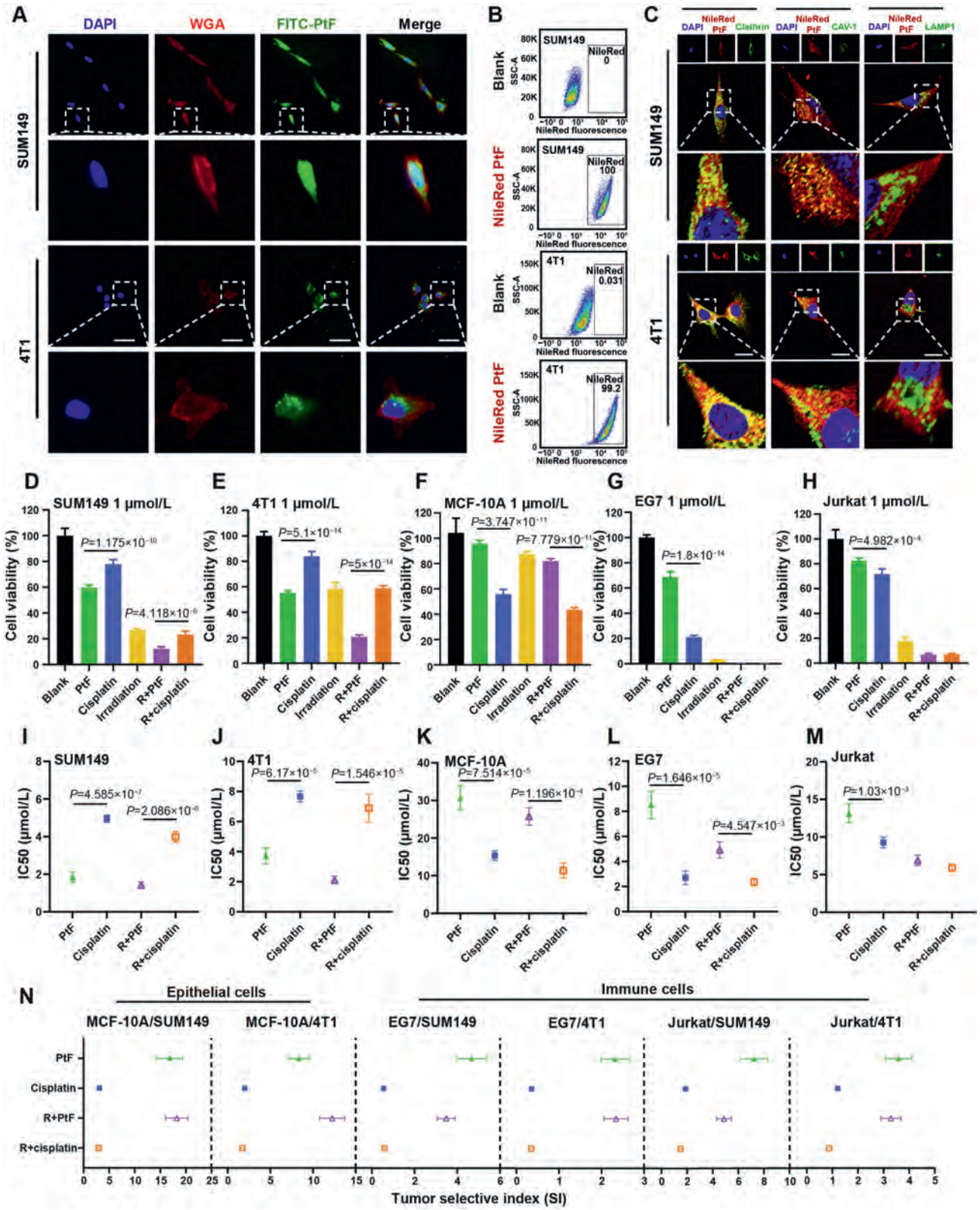

Figure 4 Biodistribution and cytotoxicity of PtF and PFD@PtF *in vitro*. (A) Subcellular biodistribution of fluorescein isothiocyanate (FITC) labeled PtF nanoparticles in SUM149 and 4T1 cells showed by confocal laser scanning microscopy images. Blue, 4′,6-diamidino-2-phenylindole (DAPI); Red, wheat germ agglutinin (WGA) 647; Green, FITC-labeled PtF. Scale bar = 50 μm. (B) The cellular internalization of NileRed-labeled PtF in SUM149 and 4T1 cells is detected by flow cytometry. (C) Co-localization of NileRed-labeled PtF nanoparticles with clathrin, caveolin-1 (CAV-1), and lysosomal associated membrane protein 1 (LAMP1) in SUM149 and 4T1 cells presented by confocal laser scanning microscopy images. Blue, DAPI; Red, NileRed-labeled PtF; Green, clathrin, caveolin-1, and LAMP1. Scale bar = 20 μm. (D–H) MTT survival

and two human cell lines (SUM149 and BT-549). After a 0.5 h incubation period, an intensive fluorescence signal of FITC is detected within the cytosol of all three cell lines, indicating that PtF nanoparticles can be promptly and efficiently uptake by TNBC cells (Fig. 4A and Supporting Information Fig. S4A). The excellent cellular uptake efficiency of PtF nanoparticles is also clearly confirmed by flow cytometry (Fig. 4B and Fig. S4B). To gain further insights into the internalization mechanism, we co-visualize the NileRed-labeled PtF with two canonical endocytosis-associated proteins (clathrin and caveolin-1) and a lysosome tracker (LAMP1) in three TNBC cell lines (SUM149, 4T1, and BT-549) (Fig. 4C and Supporting Information Fig. S5). The results show that caveolin- and clathrin-mediated endocytosis pathways are engaged in tested TNBC cell lines. It is in line with previous reports that tumor cells may internalize particles through multiple endocytosis pathways[12-14]. In addition, the obvious separation between NileRed-labeled PtF and the lysosome tracker indicates the effective escape of PtF from lysosomal entrapment, which may be potentially due to the amphiphilic features of perfluorocarbon[15-17].

To assess the cytotoxicity of synthesized PtF particles, we determine the cell viability under indicated treatment conditions with two TNBC cell lines (SUM149 and 4T1), a normal mammalian epithelial cell line (MCF-10A), and two immortalized lymphocytes (EG7 and Jurkat) using a 96 h MTT assay (Fig. 4D−H and Supporting Information Table S1). Overall, both cisplatin and PtF show tumor inhibition compared to the control group. Specifically, with or without irradiation, the prodrug PtF particles consistently show better tumor cell inhibition than cisplatin at the equimolar equivalent in TNBC cell lines. A potential explanation for the better efficacy of PtF is that the perfluorocarbon sidechains of prodrug improve the bioavailability of cisplatin by enhancing the efficiency of platinum internalization[18]. Importantly, like other prodrugs of modified cisplatin, PtF shows less toxicity in normal mammalian cells and lymphocytes. This may be attributed to the fact that the level of GSH (which triggers the release of cisplatin from prodrug) in normal cells is significantly lower compared to tumor cells (see Fig. 5D−F below). The IC_{50} of each condition above is calculated, and similar results are obtained (Fig. 4I−M and Supporting Information Table S2). The specificity and selectivity of cisplatin and PtF are evaluated by calculating the tumor-selective index (SI). Both SI on normal mammalian epithelial *vs.* tumor and SI on lymphocytes *vs.* tumor show high selectivity and tumor cell-specific toxicity (Fig. 4N). All these data suggest that PtF shows higher tumor inhibitory efficacy and lower cytotoxicity than cisplatin.

3.4. O_3_PFD@PtF and irradiation combination promote Pt releasing in vitro

We then evaluate the pharmacodynamics of ozone-loaded prodrug particles (O_3_PFD@PtF) and their combination with irradiation. Cell toxicity is evaluated using a 96 h MTT assay with indicated treatment (Fig. 5A and Supporting Information Table S3). Consistently, cisplatin and PtF show tumor inhibition in two TNBC cell lines. Compared with cisplatin or PtF, ozone-loaded PtF particle (O_3_PFD@PtF) significantly inhibits tumor cell growth. In the presence of irradiation, the efficacy of O_3_PFD@PtF is further enhanced. We then assess the synergistic effect between O_3_PFD@PtF and X-ray irradiation by figuring the combination index (CI) with the assistance of Calcusyn software (REACHSOFT, version 2.1, Beijing, China). The results show that O_3_PFD@PtF and irradiation present considerable synergistic effects in terms of cell growth inhibition across all four doses (Supporting Information Fig. S6). According to previous reports[19,20], we hypothesize that the growth inhibition induced by O_3_PFD@PtF under irradiation may be attributed to the synergistic impact of hydroxyl radicals and cisplatin. On the flip side, a large number of hydroxyl radicals generated by ozone under irradiation directly kill tumor cells. On the other hand, hydroxyl radicals indirectly promote the release of cisplatin from prodrug nanoparticles by impacting the balance of GSH-GSSG in the cytosol. Specifically, hydroxyl free radicals disrupt the intracellular redox balance and promote the generation of reducing mediators such as GSH[21]. The generated GSH subsequently releases cisplatin from prodrug PtF by reducing Pt(IV) to Pt(II).

To confirm this speculation, we visualize the ROS in three TNBC cell lines (SUM149, 4T1, and BT-549) treated with indicated conditions using a DCFH-DA fluorescence probe (Fig. 5B and Supporting Information Fig. S7A). The fluorescence signals are observed in cells treated with ozone-loaded particles in the presence or absence of X-ray irradiation. The quantification of the fluorescence signal indicates that ROS levels in cells treated with PtF and cisplatin are barely detectable, regardless of X-ray exposure (Fig. 5C and Fig. S7B). On top of O_3_PFD@PtF particles treatment, X-ray irradiation remarkably improved the ROS generation by 3.1-fold (in SUM149), 2.1-fold (in 4T1), and 3.3-fold (in BT-549). The results of intracellular ROS detection are in line with those of the extracellular hydroxyl radical generation experiment in Fig. 3G.

Then, we evaluate the impact of ROS on the intracellular balance of GSH/GSSG in tumor cells. SUM149 cells are treated with ozone-loaded perfluorodecalin emulsion (O_3_PFD emulsion) with or without irradiation. After intensive washing, the intracellular GSH and GSSG levels are measured using the DTNB (5,5′-dithiobis-(2-nitrobenzoic acid)) reduction reaction. As shown in Fig. 5D, O_3_PFD emulsion, X-ray irradiation, and their combo remarkably increase the intracellular GSH/GSSG ratio (Supporting Information Table S4). On top of this assay, we incorporate the prodrug PtF, which will release cisplatin by consuming the generated GSH (Fig. 5E). The results show that PtF, O_3_PFD@PtF, and PtF plus irradiation slightly down-regulate the GSH/GSSG ratio. On the contrary, O_3_PFD@PtF combined

assays of SUM149, 4T1, MCF-10A, EG7, and Jurkat cells after treatment with indicated regimens. Irradiation dose, 20 Gy. Data are presented as mean ± SD ($n = 6$). (D) Two-way ANOVA; PtF *vs.* Cisplatin ($P = 1.175 \times 10^{-10}$); R + PtF *vs.* R + cisplatin ($P = 4.118 \times 10^{-6}$). (E) Two-way ANOVA; PtF *vs.* Cisplatin ($P = 5.1 \times 10^{-14}$); R + PtF *vs.* R + cisplatin ($P = 5 \times 10^{-14}$). (F) Two-way ANOVA; PtF *vs.* Cisplatin ($P = 3.747 \times 10^{-11}$); R + PtF *vs.* R + cisplatin ($P = 7.779 \times 10^{-11}$). (G) Two-way ANOVA; PtF *vs.* Cisplatin ($P = 1.8 \times 10^{-14}$). (H) Two-way ANOVA; PtF *vs.* Cisplatin ($P = 4.982 \times 10^{-4}$). (I−M) The IC_{50} of indicated regimens against SUM149, 4T1, MCF-10A, EG7, and Jurkat cells. Data are presented as mean ± SD ($n = 3$). (I) Two-way ANOVA; PtF *vs.* Cisplatin ($P = 4.585 \times 10^{-7}$); R + PtF *vs.* R + cisplatin ($P = 2.086 \times 10^{-6}$). (J) Two-way ANOVA; PtF *vs.* Cisplatin ($P = 6.17 \times 10^{-5}$); R + PtF *vs.* R + cisplatin ($P = 1.546 \times 10^{-5}$). (K) Two-way ANOVA; PtF *vs.* Cisplatin ($P = 7.514 \times 10^{-5}$); R + PtF *vs.* R + cisplatin ($P = 1.196 \times 10^{-4}$). (L) Two-way ANOVA; PtF *vs.* Cisplatin ($P = 1.646 \times 10^{-5}$); R + PtF *vs.* R + cisplatin ($P = 4.547 \times 10^{-3}$). (M) Two-way ANOVA; PtF *vs.* Cisplatin ($P = 1.03 \times 10^{-3}$). (N) The tumor-selective index (SI) of indicated regimens recorded by the ratio of the IC_{50} against epithelial cells or immune cells to the IC_{50} against TNBC cells. Data are presented as mean ± SD ($n = 3$).

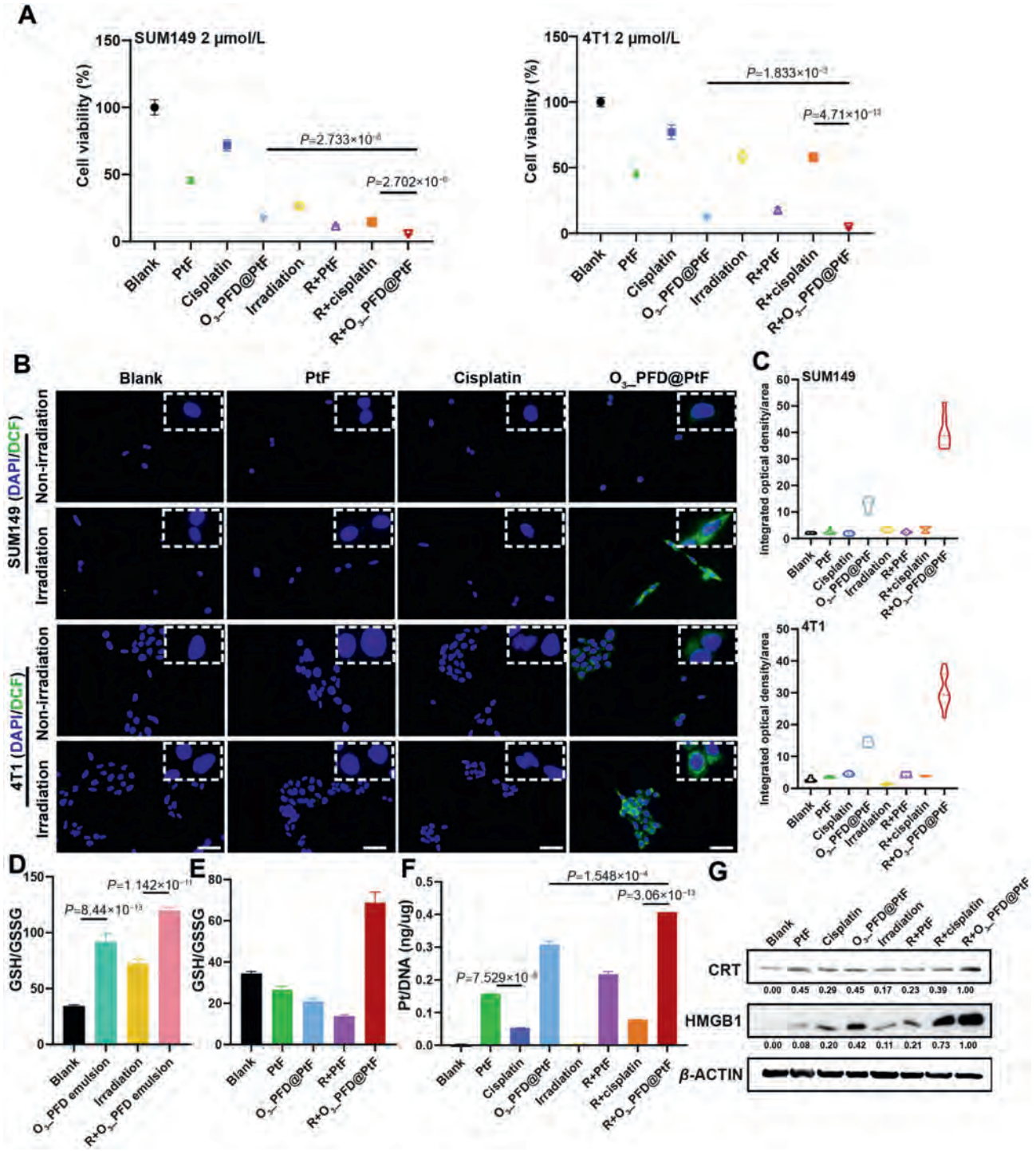

Figure 5 O_3_PFD@PtF and irradiation combination promotes Pt releasing *in vitro*. (A) MTT survival assays of SUM149, 4T1 after treatment with indicated regimens. Irradiation dose, 20 Gy. Data are presented as mean ± SD ($n = 6$). Two-way ANOVA (SUM149); O_3_PFD@PtF *vs.* R + O_3_PFD@PtF ($P = 2.733 \times 10^{-6}$); R + cisplatin *vs.* R + O_3_PFD@PtF ($P = 2.702 \times 10^{-6}$). Two-way ANOVA (4T1); O_3_PFD@PtF *vs.* R + O_3_PFD@PtF ($P = 1.833 \times 10^{-3}$); R + cisplatin *vs.* R + O_3_PFD@PtF ($P = 4.71 \times 10^{-13}$). (B) The intracellular reactive oxygen species (ROS) in SUM149 and 4T1 cells treated with indicated regimens are probed with 2,7-dichlorodihydrofluorescein diacetate (DCFH-DA). Blue, 4′,6-diamidino-2-phenylindole (DAPI); Green, dichlorofluorescein (DCF). Scale bar = 50 μm. (C) Quantification of DCF fluorescence intensity by integrated optical density/area. (D) The intracellular reduced glutathione/oxidized glutathione (GSH/GSSG) ratio in SUM149 cells treated with O_3_PFD emulsion with or without irradiation. Data are presented as mean ± SD ($n = 3$). Two-way ANOVA; Blank *vs.* O_3_PFD emulsion ($P = 8.44 \times 10^{-13}$); Irradiation *vs.* R + O_3_PFD emulsion ($P = 1.142 \times 10^{-11}$). (E) The intracellular GSH/GSSG ratio in SUM149 cells treated with PtF nanoparticles and O_3_PFD@PtF nanoparticles with or without irradiation. Data are presented as mean ± SD ($n = 3$). (F) Content of platinum (Pt) element inserted in DNA of SUM149 cells treated with indicated regimens. Data are presented as mean ± SD ($n = 3$). Two-way

with irradiation dramatically upregulates the GSH/GSSG ratio. This suggests that the combination of ozone and X-ray irradiation, rather than each single treatment, maintains a high level of GSH. As a result, the released cisplatin will incorporate into chromosome DNA and form a Pt−DNA complex. We then extracted the nucleus DNA and measured the DNA-bond platinum. Not surprisingly, the amount of DNA-bound platinum is consistent with the ratio of GSH/GSSG (Fig. 5F and Supporting Information Table S5).

As reported previously, cisplatin alone is not effective in triggering ICD because it cannot translocate the antigen-carried CRT to the surface of the cell. However, ROS promotes CRT translocation. Thus, in our design rationale, the ozone-derived ROS may serve as an enhancer for ICD induced by cisplatin. To validate this principle, we examine the levels of two ICD markers, HMGB1 and CRT, in SUM149 cells exposed to PtF, cisplatin, and O_3_PFD@PtF with or without irradiation (Fig. 5G). Upon irradiation, cisplatin leads to an upregulated CRT expression, likely attributed to the generation of ROS by X-ray. Furthermore, O_3_PFD@PtF treatment in combination with irradiation exhibits even higher CRT exposure compared to cisplatin plus irradiation. This may be attributed to the differential efficiency of ROS production with or without ozone in the presence of irradiation. Similarly, O_3_PFD@PtF administration significantly increases the expression levels of HMGB1, particularly when combined with irradiation.

3.5. O_3_PFD@PtF and irradiation combination inhibit tumor growth

Encouraged by the remarkable efficacy and selectivity observed *in vitro*, we proceed with evaluating the *in vivo* antitumor efficiency of the prodrug nanosystem. We characterize the biodistribution of PtF nanoparticles by intravenously injecting NileRed-labeled PtF nanoparticles into 4T1-bearing mice. The fluorescence signals of NileRed in dissected major organs and tumors are recorded at four indicated time points (1, 6, 12, and 24 h) utilizing IVIS Spectrum. The PtF particles are observed in tumor mass as early as 1 h after injection, and they continue to accumulate for at least 24 h (Fig. 6A and B), indicating that PtF is a tumor-targeted carrier with long-lasting accumulation properties. Additionally, strong fluorescence signals are observed in the liver and kidneys at 1 h, followed by a significant decrease within 24 h post-injection. This suggests that PtF nanoparticles primarily undergo hepatic and renal metabolic pathways, followed by a quick bio-elimination.

We then evaluate the antitumor efficacy of indicated regimens on a BALB/c mice model with unilateral subcutaneous 4T1 xenografts (Fig. 6C). Briefly, tumor-bearing mice are randomly divided into 8 groups and administered with indicated regimens respectively, including PBS (Blank), PtF, cisplatin, O_3_PFD@PtF, PBS plus X-ray irradiation (Irradiation), PtF plus X-ray irradiation (R + PtF), cisplatin plus X-ray irradiation (R + cisplatin), and O_3_PFD@PtF plus X-ray irradiation (R + O_3_PFD@PtF). Tumor volumes and body weight are monitored throughout the experiment to profile tumor growth curves and alterations of body weight, respectively (Fig. 6D and E). After 3 dosages of treatment, tumors from each experimental group are excised, photographed, and weighed (Fig. 6F and G; Supporting Information Table S6) on Day 26 upon inoculation. The results of the tumor growth curve and tumor weight show that each single treatment (PtF, cisplatin, and O_3_PFD@PtF) shows effective tumor inhibition compared with the blank group. The inhibition can be further improved by the combination of X-ray irradiation. Remarkably, the combination of O_3_PFD@PtF and X-ray irradiation shows the most powerful inhibition of tumor growth among all groups.

These results are further confirmed on an independent bilateral subcutaneous 4T1-Luc xenografted mice model. Tumor-bearing mice are treated with indicated regimens, and X-ray irradiation is performed on the primary tumors (right side) as needed. At the endpoint of the experiment, tumors are visualized *in situ* using bioluminescent *in vivo* imaging (Supporting Information Fig. S8A). Not surprisingly, similar results of tumor inhibition in the unilateral model are obtained on the primary tumor from the bilateral model. In addition, comparable tumor inhibition is observed between the primary and abscopal tumors treated with indicated regimens except for tumors treated with irradiation alone (Figs. S8B and C; Supporting Information Table S7). Primary tumor rather than abscopal tumor responses to the irradiation. The results suggest that irradiation alone cannot effectively elicit an abscopal effect.

Despite its high efficacy, the prodrug nano system offers the advantage of reducing the systemic toxicity associated with cisplatin and radiotherapy, as proven *in vitro* (Fig. 4D−N). Here, this advantage is further confirmed *in vivo*. As shown in Fig. 6E, mice treated with cisplatin experience body weight loss, regardless of whether it is combined with X-ray irradiation or not. To specify the systemic toxicity, we profile the body weight at the endpoint of the experiment (Fig. 6H and Supporting Information Table S8). Compared to free cisplatin, the prodrug PtF significantly alleviates chemo-induced toxicity, regardless of X-ray irradiation. At the end of the experiment, important organs like the heart, liver, spleen, lung, and kidney are collected, along with peripheral blood samples for hematological and pathological assessment. No visible histological damage is observed in the tissue slides derived from each group except for the kidney slides from the cisplatin-treated group (Supporting Information Fig. S9). The kidneys from the cisplatin-treated group exhibit obvious glomerular fusion and atrophy, which are typical signs of kidney damage. Remarkably, these pathological morphologies are not observed in the kidneys of mice receiving prodrug nanoparticle treatment. The cisplatin-related toxicities are further confirmed by the hematologic and biochemical analysis. Consistent with the H&E staining results, abnormally high levels of urea (UREAL) are observed in mice treated with cisplatin and cisplatin plus irradiation (Supporting Information Fig. S10). These findings collectively indicate that the prodrug nano system PtF effectively avoids systemic toxicity induced by cisplatin. Meanwhile, the combination regimen of O_3_PFD@PtF and X-ray irradiation exhibits both efficient tumor inhibition and commendable biosafety in animal experiments.

To elucidate the molecular mechanisms behind tumor growth inhibition, we evaluate the histopathology of tumors treated with indicated regimens using H&E staining (Fig. 7A). We observe similar degrees of tumor tissue damages, as indicated by karyopyknosis and disruption of intercellular junctions, in tumors treated with cisplatin

ANOVA; PtF *vs.* Cisplatin ($P = 7.529 \times 10^{-8}$); O_3_PFD@PtF *vs.* R + O_3_PFD@PtF ($P = 1.548 \times 10^{-4}$); R + cisplatin *vs.* R + O_3_PFD@PtF ($P = 3.06 \times 10^{-13}$). (G) Western blot of ICD markers (CRT and HMGB1) in SUM149 cells treated with indicated regimens. β-ACTIN protein served as the loading control. CRT, calreticulin. HMGB1, high mobility group box 1.

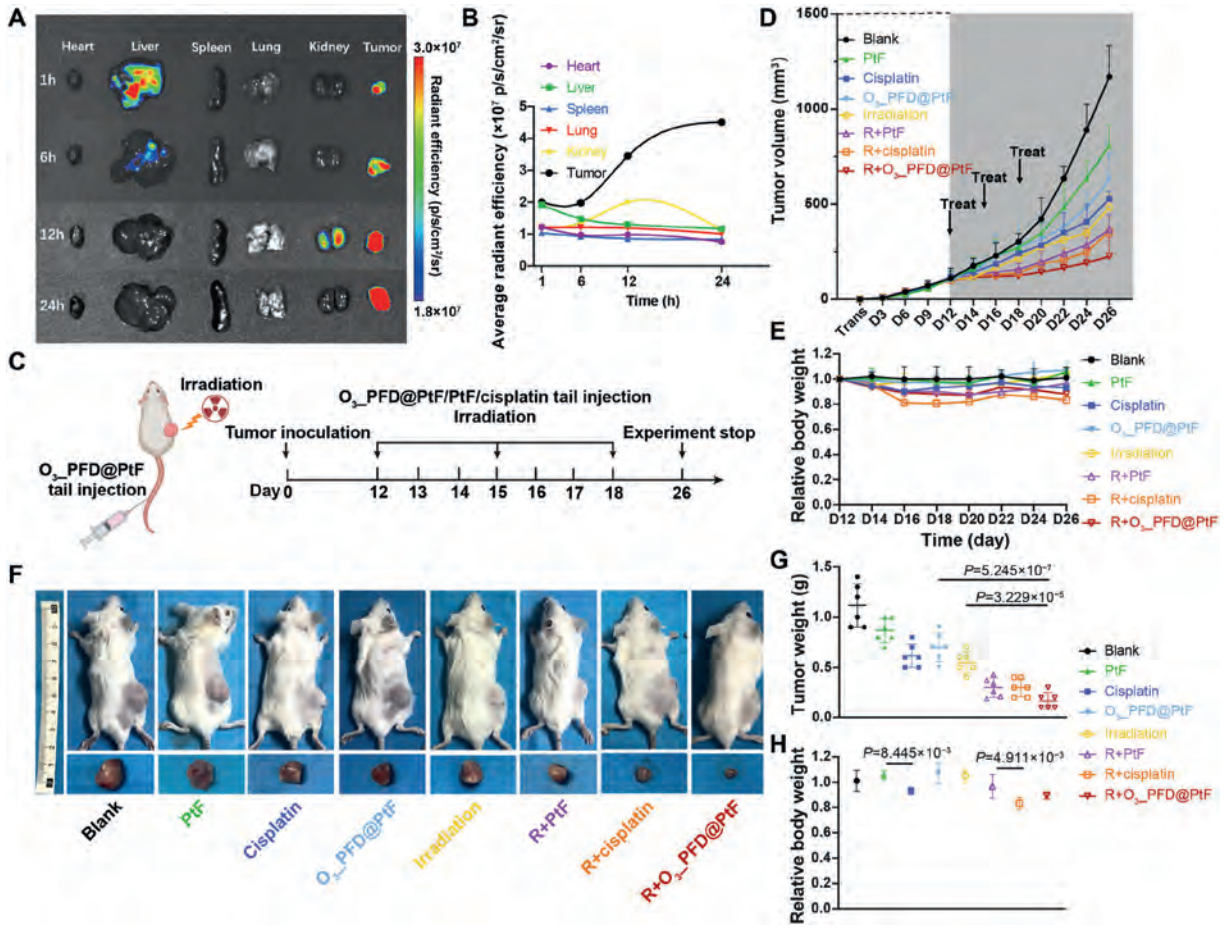

Figure 6 O_3_PFD@PtF and irradiation combination inhibit tumor growth. (A) Biodistribution of NileRed-labeled PtF in 4T1 tumor mice model at indicated time points after intravenous administration. (B) Quantitative assessment of fluorescence signal in heart, liver, spleen, lung, kidney, and tumor at indicated time points. (C) Treatment schema for subcutaneous 4T1 xenografted mice model (Created with BioRender.com). (D) Tumor growth curves of indicated treatment groups. (E) Body weight change curves of mice in indicated treatment groups. (F) Photographs of mice and dissected tumors. (G) Weight of tumors in indicated treatment groups. Data are exhibited as mean ± SD ($n = 6$). Two-way ANOVA; O_3_PFD@PtF *vs.* R + O_3_PFD@PtF ($P = 5.245 \times 10^{-7}$); Irradiation *vs.* R + O_3_PFD@PtF ($P = 3.229 \times 10^{-5}$). (H) Body weight of mice in indicated treatment groups at the endpoint of the experiment. Data are exhibited as mean ± SD ($n = 6$). Two-way ANOVA; PtF *vs.* Cisplatin ($P = 8.445 \times 10^{-3}$); R + PtF *vs.* R + cisplatin ($P = 4.911 \times 10^{-3}$).

and prodrug PtF. Loading with ozone, O_3_PFD@PtF clearly enhances the tumor damage. These damages are further improved by X-ray irradiation. The most severe histological damage is observed in the tumors treated with O_3_PFD@PtF plus irradiation. Consistently, the index of cell apoptosis, indicated by markers BAX and Cleaved caspase-3, also shows similar trends as that in the histological analysis (Fig. 7B, C, E, F and Supporting Information Table S9). Remarkably, the combination of O_3_PFD@PtF and X-ray irradiation results in very high levels of apoptotic signals, implying a severe ICD. Moreover, the number of proliferative cells, indicated by Ki67 expression, shows an opposite pattern (Fig. 7D, G and Table S9). Treatment with cisplatin, PtF, and O_3_PFD@PtF significantly reduces the Ki67-positive cell number compared to the control group. Tumor cell proliferation is further attenuated by the combination of X-ray irradiation. Almost no Ki67-positive cells are observed in tumors treated with the combo regimen of O_3_PFD@PtF and X-ray irradiation.

Encouraged by the excellent inhibitory effect of this combo regimen on the subcutaneous xenograft tumor model, we further validate the antitumor efficacy on a 4T1-Luc lung metastatic mice model (Fig. 8A). The lung metastatic tumor is monitored by bioluminescence imaging, and the tumor growth curves are profiled accordingly (Fig. 8B and C). After 3 dosages of treatment, the mice are euthanized, and the lungs are harvested on Day 13 upon inoculation. The number of lung metastatic lesions is evaluated with H&E staining of tumor sections (Fig. 8D and E and Supporting Information Table S10). The results indicate that the mono-drug treatment (Cisplatin, PtF, or O_3_PFD@PtF) shows moderate efficacy in inhibiting lung metastasis compared to the blank group. And the tumor inhibitory efficacy is further boosted by irradiation. The combo of O_3_PFD@PtF and X-ray irradiation exhibits the highest efficacy in suppressing lung metastasis among the tested regimens.

3.6. Combo of O_3_PFD@PtF and irradiation improved immune-related cell death

As programmed cell death is usually correlated with ICD, we then investigate the intensity of ICD in tumors that are treated with indicated regimens. The ICD levels are evaluated by examining canonical biomarkers, including CRT, HMGB1, and HSP70 (Fig. 9A–F and Supporting Information Table S11). In

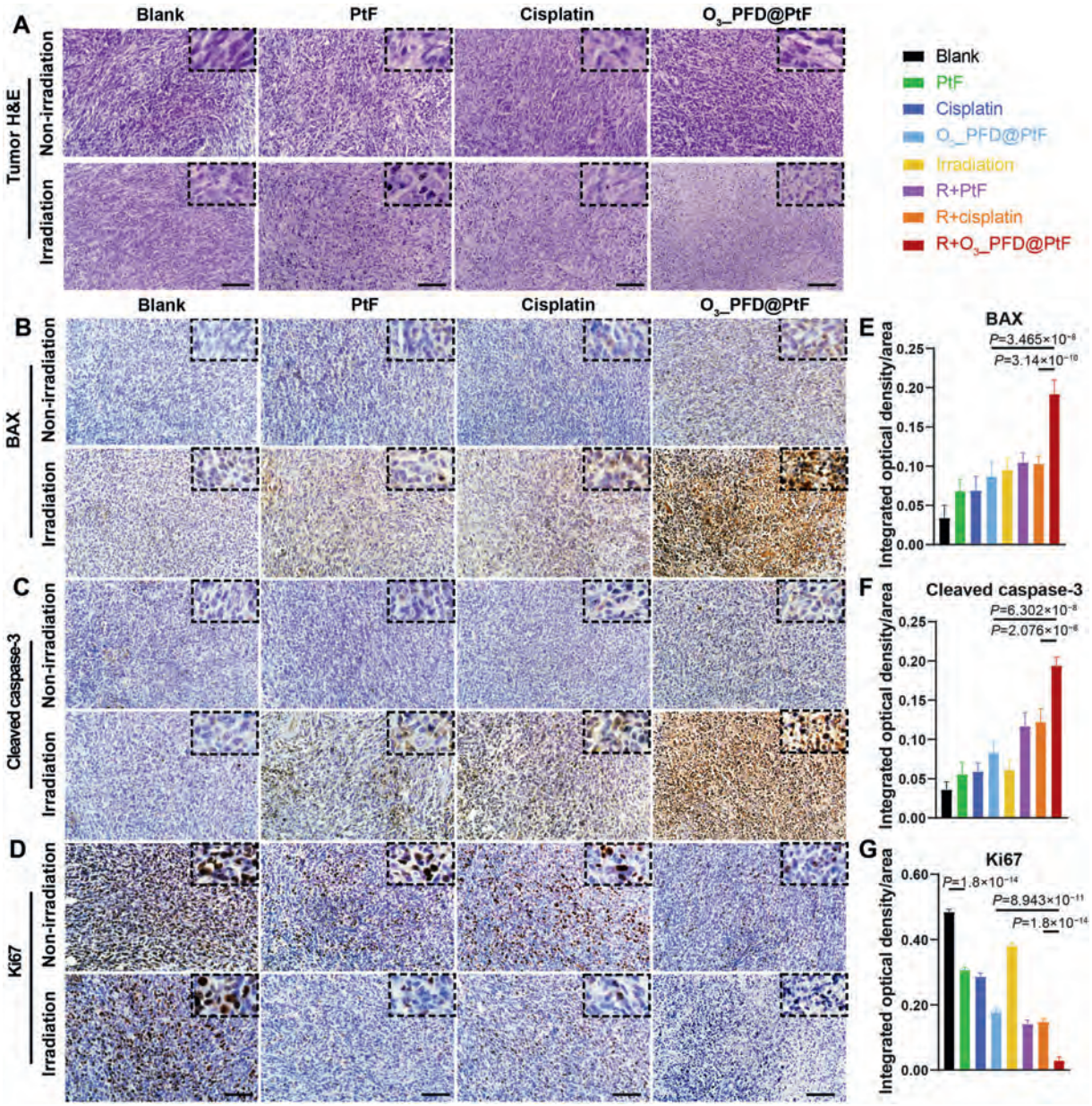

Figure 7 Assessment of apoptosis and necrosis in tumors. (A) Hematoxylin−eosin (H&E) staining of tumor tissue slides from mice treated with indicated regimens. Scale bar = 100 μm. (B−D) Immunohistochemical evaluation of BAX, Cleaved caspase-3, and Ki67 expression levels in tumors from indicated groups of mice. Scale bar = 100 μm. (E−G) The staining intensities of BAX, Cleaved caspase-3, and Ki67 are quantified by integrated optical density/area. Data are presented as mean ± SD (n = 4). (E) Two-way ANOVA; O_3_PFD@PtF *vs.* R + O_3_PFD@PtF ($P = 3.465 \times 10^{-8}$); R + cisplatin *vs.* R + O_3_PFD@PtF ($P = 3.14 \times 10^{-10}$). (F) Two-way ANOVA; O_3_PFD@PtF *vs.* R + O_3_PFD@PtF ($P = 6.302 \times 10^{-8}$); R + cisplatin *vs.* R + O_3_PFD@PtF ($P = 2.076 \times 10^{-8}$). (G) Two-way ANOVA; Blank *vs.* PtF ($P = 1.8 \times 10^{-14}$); O_3_PFD@PtF *vs.* R + O_3_PFD@PtF ($P = 8.943 \times 10^{-11}$); R + cisplatin *vs.* R + O_3_PFD@PtF ($P = 1.8 \times 10^{-14}$).

comparison with the control group, the results from IHC staining and integrated optical density/area quantification demonstrate that cisplatin, PtF, and O_3_PFD@PtF induce a slight increase in ICD. The ICD is further enhanced by the combination of X-ray irradiation. The most severe ICD is observed in tumors treated with irradiation plus O_3_PFD@PtF. Theoretically, ICD can improve neoantigen exposure and T lymphocyte infiltration into the tumors. As a result, we evaluate the levels of $CD4^+$ and $CD8^+$ T lymphocytes in tumors by IF staining and flow cytometry (Fig. 9G−M, Supporting Information Tables S12 and S13). The results show similar trends to those observed in ICD marker measurements. Treatment with cisplatin, PtF, and O_3_PFD@PtF significantly increases the densities of tumor-infiltrated lymphocytes, which are further improved by the combination of X-ray irradiation. Taken together, the combination of irradiation with an ozone-loaded prodrug nanosystem can significantly suppress tumor proliferation by inducing apoptotic-related ICD, which not only efficiently inhibits tumor growth but also provides a promising fundament for combination with immunotherapy.

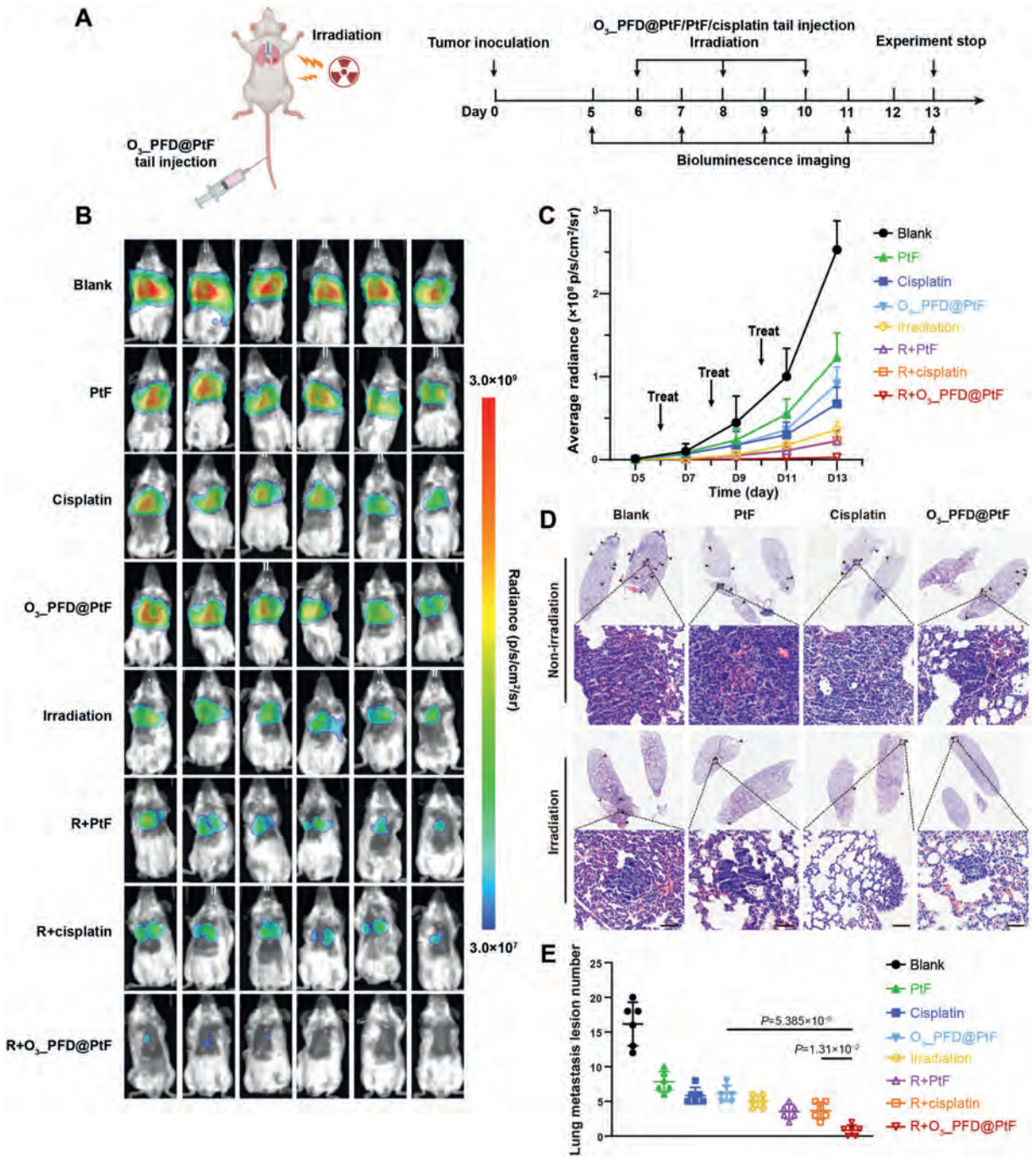

Figure 8 O_3_PFD@PtF and irradiation combination inhibit lung metastasis tumor growth. (A) Treatment schema for luciferase-expressing 4T1 lung metastatic mice model (Created with BioRender.com). (B) Bioluminescence images of mice with lung metastasis tumors in the indicated treatment groups at the endpoint of the experiment. (C) Lung metastasis tumor growth curves plotted by quantitative analysis of bioluminescence intensities. Data are presented as mean ± SD ($n = 6$). (D) H&E staining of pulmonary tissues from mice treated with indicated regimens. Scale bar = 100 μm. (E) The number of lung metastasis lesions counted based on the H&E staining of lung tissues. Data are exhibited as mean ± SD ($n = 6$). Two-way ANOVA; O_3_PFD@PtF *vs.* R + O_3_PFD@PtF ($P = 5.385 \times 10^{-5}$); R + cisplatin *vs.* R + O_3_PFD@PtF ($P = 1.31 \times 10^{-2}$).

4. Discussion

Although the combination of chemotherapy and radiotherapy shows promising outcomes in clinics, several defects, including intolerable systematic toxicity, as well as hypoxic and unfavorable immune microenvironments, severely dampen its application[22,23]. Therefore, enhancing therapeutic effects and reducing systematic toxicity are two critical issues in cancer therapy. To address these challenges, researchers have focused on improving the efficacy of combined therapy for cancer treatment by alleviating hypoxia[24] and sensitizing chemotherapy[25]. With the advancement of anti-tumor strategies, various gases have been identified to possess outstanding antitumor effects while maintaining superior safety profiles[26]. In this manuscript, we present a self-assembling ozone

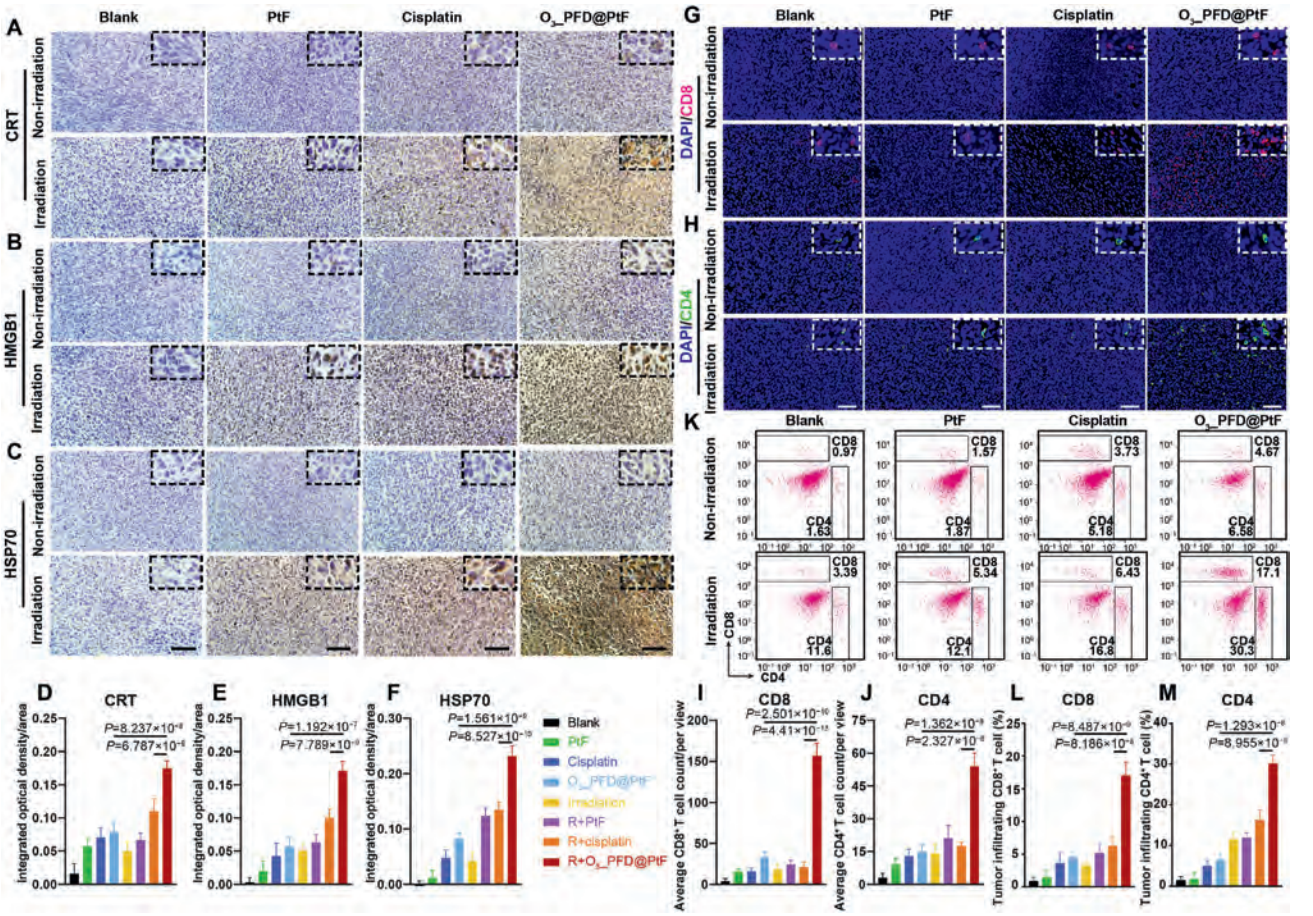

Figure 9 Assessment of immunogenic cell death and tumor-infiltrating T-cells. (A−C) Immunohistochemical evaluation of calreticulin (CRT), high mobility group box 1 (HMGB1), and heat shock protein70 (HSP70) expression levels in tumors from indicated groups of mice. Scale bar = 100 μm. (D−F) The staining intensities of CRT, HMGB1, and HSP70 are quantified by integrated optical density/area. Data are presented as mean ± SD (n = 4). (D) Two-way ANOVA; O_3_PFD@PtF *vs.* R + O_3_PFD@PtF ($P = 8.237 \times 10^{-8}$); R + cisplatin *vs.* R + O_3_PFD@PtF ($P = 6.787 \times 10^{-9}$). (E) Two-way ANOVA; O_3_PFD@PtF *vs.* R + O_3_PFD@PtF ($P = 1.192 \times 10^{-7}$); R + cisplatin *vs.* R + O_3_PFD@PtF ($P = 7.789 \times 10^{-9}$). (F) Two-way ANOVA; O_3_PFD@PtF *vs.* R + O_3_PFD@PtF ($P = 1.561 \times 10^{-9}$); R + cisplatin *vs.* R + O_3_PFD@PtF ($P = 8.527 \times 10^{-10}$). (G, H) Immunofluorescence staining of tumor-infiltrating T lymphocytes. Blue, 4′,6-diamidino-2-phenylindole (DAPI); Red, CD8; Green, CD4. Scale bar = 100 μm. (I, J) Quantitative evaluation of $CD8^+$ and $CD4^+$ T lymphocytes in each area of view. Data are presented as mean ± SD (n = 4) (I) Two-way ANOVA; O_3_PFD@PtF *vs.* R + O_3_PFD@PtF ($P = 2.501 \times 10^{-10}$); R + cisplatin *vs.* R + O_3_PFD@PtF ($P = 4.41 \times 10^{-13}$). (J) Two-way ANOVA; O_3_PFD@PtF *vs.* R + O_3_PFD@PtF ($P = 1.362 \times 10^{-8}$); R + cisplatin *vs.* R + O_3_PFD@PtF ($P = 2.327 \times 10^{-8}$). (K) Flow cytometry analysis of $CD8^+$ and $CD4^+$ T-cells infiltrating the tumor. (L, M) Percentage of $CD8^+$ and $CD4^+$ T-cells among $CD3^+$ T-cells plotted based on flow cytometry analysis. Data are presented as mean ± SD (n = 6). (L) Two-way ANOVA; O_3_PFD@PtF *vs.* R + O_3_PFD@PtF ($P = 8.487 \times 10^{-9}$); R + cisplatin *vs.* R + O_3_PFD@PtF ($P = 8.186 \times 10^{-8}$). (M) Two-way ANOVA; O_3_PFD@PtF *vs.* R + O_3_PFD@PtF ($P = 1.293 \times 10^{-8}$); R + cisplatin *vs.* R + O_3_PFD@PtF ($P = 8.955 \times 10^{-8}$).

delivery nanosystem consisting of fluorocarbon chain-modified cisplatin prodrug. The advantages of this system are 1) reducing toxicity, 2) improving the efficacy of chemo plus radiotherapy, and 3) providing an immune-favored niche.

Cisplatin is commonly used as a cornerstone chemotherapeutic drug for TNBC in clinical practice[27]. However, its broad application is hindered by severe dose-limiting toxicities, such as nephrotoxicity and ototoxicity[28]. Multiple nano-based platinum(IV) prodrugs have been developed[29-31] to alleviate the side effects of cisplatin. In our nanosystem, the platinum is modified as a reduction-responsive Pt(IV) prodrug, which can be specifically released by GSH. GSH is a natural byproduct in mammalian cells and is essential for antioxidant defense, proliferation, cell differentiation, and apoptosis[32]. Compared with extracellular matrix or blood circulation, cytosolic GSH concentration is around 100−1000 times higher[33]. To neutralize severe oxidative stress, tumor cells typically generate more GSH (2−10 mmol/L, approximately 4 times higher) than normal cells do, which fortunately serves as a tumor-specific stimulus for cisplatin release from prodrug PtF[34]. The up-regulation of GSH in tumor cells is further augmented by the ozone loaded into the particle[35]. Thus, the prodrug shows less systematic toxicity in both *in vitro* experiments and *in vivo* experiments.

Our prodrug nano system potently improves the efficacy of chemo plus radiotherapy. Firstly, the fluorocarbon chains of prodrug PtF enhance bioavailability by facilitating the drug transmembrane[36,37]. Secondly, the release efficiency of cisplatin from PtF prodrug can be augmented by combining ozone and X-ray irradiation. Specifically, the loaded ozone in PFD@PtF can generate ROS upon exposure to X-ray irradiation[19,38]. The

elevated level of ROS induces oxidative stress in tumor cells, resulting in the upregulation of the intracellular GSH/GSSG ratio[21]. As a result, the generated GSH facilitates the reduction-responsive release of cisplatin from the prodrug. Thirdly, oxygen produced by ozone under irradiation can alleviate the hypoxic conditions in the tumor microenvironment, enhancing the effectiveness of radiotherapy[39,40].

The promising outcomes of immunotherapy in treating solid tumors have drawn large attention to its application in TNBC. Previous research has confirmed that certain nanomaterials can induce ICD and enhance the immune response against tumor cells[41]. In our study, we observe that the Pt(IV) prodrug nanosystem also provides a fundament for combination with immunotherapy in the future. The combo regimen is promising for enhancing antitumor immune response because it potently induces ICD and promotes the proliferation of lymphocytes. Firstly, radiotherapy induces ICD by producing ROS and increasing neoantigen generation[42]. On this basis, ozone plus X-ray irradiation generates even more ROS in tumors, greatly eliciting a burst of ICD by inducing endoplasmic reticulum stress (ERS) and CRT exposure in tumor cells[43]. Secondly, although certain chemo drugs also have the ability to induce ICD[44,45], cisplatin has been reported to fail in inducing ICD because of inadequate CRT exposure[46]. Since both ATP and HMGB1 release can be enhanced by cisplatin, combining a CRT exposure inducer with cisplatin holds promise in achieving full-blown ICD[46,47]. Therefore, the combination of ozone and cisplatin released by Pt(IV) prodrug shows synergistic induction of ICD under X-ray irradiation. Finally, as a side product, the oxygen derived from ozone contributes to the creation of an immune-favored microenvironment by alleviating hypoxia, which supports lymphocyte proliferation[48,49].

In this manuscript, we attempt to utilize perfluorooctanoate as the axial ligand of platinum(IV) and employ the cisplatin prodrug to construct a carrier-free ozone delivery nanosystem. In this system, the prodrug Pt(IV)-PFOA itself serves as a unit of the vehicle. By incorporating the fluorocarbon chain, the Pt(IV) prodrug has the capability to self-assemble into nanoparticles *via* hydrophobic interactions, significantly reducing the need for excipients and mitigating polymer-related toxicity[50]. The carrier-free nature of the Pt(IV) prodrug nanoparticle endows the system with an exceptionally high drug-loading capacity. As summarized by several reviews, the simplified self-assembling of micelle nanoparticles with prodrug potentially addresses the limitation of conventional nanoformulations in terms of mass production and quality control[51-53], which indicates expected clinic-translational potency in the future.

5. Conclusions

In conclusion, we successfully developed a smart self-assembled nano micelle consisting of carrier-free cisplatin prodrug to deliver a gaseous drug into tumor masses. By loading ozone, the nanosystem efficiently suppresses tumor growth in an on-demand cisplatin release pattern upon X-ray irradiation. This prodrug nano system offers a promising approach to synchronize radiotherapy and chemotherapy applications in TNBC without significant systemic toxicity.

Acknowledgments

This study was supported by Noncommunicable Chronic Diseases-National Science and Technology Major Project (2023ZD0502300 [2023ZD0502304], China), National Guidance Fund on Developing Local Science and Technology for Sichuan Province (2023ZYD0167, China), the National Key Research and Development Program of China (2022YFA1207300 [2022YFA1207303], China), National Natural Science Foundation of China (No. 82172634, China), Key Program of the Science and Technology Bureau of Sichuan (No. 2021YFSY0007, China), 1.3.5 project for disciplines of excellence, West China Hospital, Sichuan University (No. ZYGD23028, China), Sichuan Province Health Commission (JH20231197, China), and Dedicated Postdoctoral R&D Fund, West China Hospital, Sichuan University (2023HXBH132, China). The authors thank Huifang Li (Cytology and Molecular Platform, Core Facilities of West China Hospital) for her contribution to this study.

Author contributions

Tianyue Xu: Writing − original draft, Visualization, Validation, Methodology, Investigation, Formal analysis, Conceptualization. Dan Zheng: Writing − original draft, Visualization, Validation, Methodology, Investigation, Formal analysis, Conceptualization. Meixu Chen: Writing − original draft, Visualization, Validation, Methodology, Investigation, Formal analysis. Linlin Song: Methodology, Investigation. Zhihui Liu: Methodology, Investigation. Yan Cheng: Methodology, Investigation. Yujie Zhao: Methodology, Investigation. Liwen Huang: Investigation. Yixuan Li: Investigation. Zhankun Yang: Writing − review & editing. Cong Li: Methodology. Biao Dong: Writing − review & editing, Supervision, Project administration, Funding acquisition. Jing Jing: Writing − review & editing, Supervision, Project administration, Funding acquisition. Hubing Shi: Writing − review & editing, Writing − original draft, Supervision, Project administration, Funding acquisition, Conceptualization.

Conflicts of interest

The authors have no conflicts of interest to declare.

Declaration of Generative AI and AI-assisted technologies in the writing process

During the preparation of this work the authors used ChatGPT 3.5 in order to refine the English quality. After using this tool, the authors reviewed and edited the content as needed and take full responsibility for the content of the publication.

Appendix A. Supporting information

Supporting Information to this article can be found online at https://doi.org/10.1016/j.apsb.2025.03.020.

References

1. McDonald ES, Clark AS, Tchou J, Zhang P, Freedman GM. Clinical diagnosis and management of breast cancer. *J Nucl Med* 2016; **57**(Suppl 1):9S−16S.
2. Bianchini G, De Angelis C, Licata L, Gianni L. Treatment landscape of triple-negative breast cancer—expanded options, evolving needs. *Nat Rev Clin Oncol* 2022;**19**:91−113.
3. Pabla N, Dong Z. Cisplatin nephrotoxicity: mechanisms and renoprotective strategies. *Kidney Int* 2008;**73**:994−1007.

4. Kerr AJ, Dodwell D, McGale P, Holt F, Duane F, Mannu G, et al. Adjuvant and neoadjuvant breast cancer treatments: a systematic review of their effects on mortality. *Cancer Treat Rev* 2022;**105**:102375.
5. Speers C, Pierce LJ. Postoperative radiotherapy after breast-conserving surgery for early-stage breast cancer: a review. *JAMA Oncol* 2016;**2**:1075−82.
6. Nagasawa S, Takahashi J, Suzuki G, Hideya Y, Yamada K. Why concurrent CDDP and radiotherapy has synergistic antitumor effects: a review of *in vitro* experimental and clinical-based studies. *Int J Mol Sci* 2021;**22**:3140.
7. Forastiere AA, Zhang Q, Weber RS, Maor MH, Goepfert H, Pajak TF, et al. Long-term results of RTOG 91-11: a comparison of three nonsurgical treatment strategies to preserve the larynx in patients with locally advanced larynx cancer. *J Clin Oncol* 2013;**31**:845−52.
8. Takada M, Fukuoka M, Kawahara M, Sugiura T, Yokoyama A, Yokota S, et al. Phase III study of concurrent *versus* sequential thoracic radiotherapy in combination with cisplatin and etoposide for limited-stage small-cell lung cancer: results of the Japan Clinical Oncology Group Study 9104. *J Clin Oncol* 2002;**20**:3054−60.
9. Forastiere AA, Goepfert H, Maor M, Pajak TF, Weber R, Morrison W, et al. Concurrent chemotherapy and radiotherapy for organ preservation in advanced laryngeal cancer. *N Engl J Med* 2003;**349**:2091−8.
10. Li Y, Wang J, Ma XW, Tan L, Yan YL, Xue CF, et al. A review of neoadjuvant chemoradiotherapy for locally advanced rectal cancer. *Int J Biol Sci* 2016;**12**:1022−31.
11. Hickey BE, Francis DP, Lehman M. Sequencing of chemotherapy and radiotherapy for early breast cancer. *Cochrane Database Syst Rev* 2013;**30**:CD005212.
12. Rejman J, Bragonzi A, Conese M. Role of clathrin-and caveolae-mediated endocytosis in gene transfer mediated by lipo-and polyplexes. *Mol Ther* 2005;**12**:468−74.
13. Mathew B, Ravindran S, Liu XR, Torres L, Chennakesavalu M, Huang CC, et al. Mesenchymal stem cell-derived extracellular vesicles and retinal ischemia-reperfusion. *Biomaterials* 2019;**197**:146−60.
14. Liu Y, Luo JS, Liu YJ, Liu W, Yu GT, Huang YT, et al. Brain-targeted biomimetic aanodecoys with neuroprotective effects for precise therapy of Parkinson's disease. *ACS Cent Sci* 2022;**8**:1336−49.
15. Lv J, Wang H, Rong GY, Cheng YY. Fluorination promotes the cytosolic delivery of genes, proteins, and peptides. *Acc Chem Res* 2022;**55**:722−33.
16. Wei YS, Li XD, Lin JH, Zhou Y, Yang JD, Hou MY, et al. Oral delivery of siRNA using fluorinated, small-sized nanocapsules toward anti-inflammation treatment. *Adv Mater* 2023;**35**:2206821.
17. Liu Y, Zhang J, Tu Y, Zhu L. Potential-independent intracellular drug delivery and mitochondrial targeting. *ACS Nano* 2021;**16**:1409−20.
18. Riess JG. Highly fluorinated amphiphilic molecules and self-assemblies with biomedical potential. *Curr Opin Colloid Interf Sci* 2009;**14**:294−304.
19. Zheng D, Li YC, Song LL, Xu TY, Jiang X, Yin XM, et al. Improvement of radiotherapy with an ozone-carried liposome nanosystem for synergizing cancer immune checkpoint blockade. *Nano Today* 2022;**47**:101675.
20. Song LL, Zheng D, Xu JS, Xu TY, Liu ZH, Zhang H, et al. Improvement of TNBC immune checkpoint blockade with a microwave-controlled ozone release nanosystem. *J Control Release* 2022;**351**:954−69.
21. Ju EG, Dong K, Chen ZW, Liu Z, Liu CQ, Huang YY, et al. Copper (II)−graphitic carbon nitride triggered synergy: improved ROS generation and reduced glutathione levels for enhanced photodynamic therapy. *Angew Chem Int Ed Engl* 2016;**55**:11467−71.
22. Xie JN, Gong LJ, Zhu S, Yong YA, Gu ZJ, Zhao YL. Emerging strategies of nanomaterial-mediated tumor radiosensitization. *Adv Mater* 2019;**31**:1802244.
23. Li Y, Zhang HJ, Merkher Y, Chen L, Liu N, Leonov S, et al. Recent advances in therapeutic strategies for triple-negative breast cancer. *J Hematol Oncol* 2022;**15**:121.
24. Gou SQ, Chen NX, Wu XA, Zu MH, Yi SX, Ying BW, et al. Multi-responsive nanotheranostics with enhanced tumor penetration and oxygen self-producing capacities for multimodal synergistic cancer therapy. *Acta Pharm Sin B* 2022;**12**:406−23.
25. Yang Y, Hu DR, Lu Y, Chu BY, He XL, Chen Y, et al. Tumor-targeted/reduction-triggered composite multifunctional nanoparticles for breast cancer chemo-photothermal combinational therapy. *Acta Pharm Sin B* 2022;**12**:2710−30.
26. Lin CC, Huang CY, Shi ZQ, Ou MT, Sun SJ, Yu M, et al. Biodegradable calcium sulfide-based nanomodulators for H_2S-boosted Ca^{2+}-involved synergistic cascade cancer therapy. *Acta Pharm Sin B* 2022;**12**:4472−85.
27. Telli ML, Gradishar WJ, Ward JH. NCCN guidelines updates: breast cancer. *J Natl Compr Canc Netw* 2019;**17**:552−5.
28. Trendowski MR, El Charif O, Dinh Jr PC, Travis LB, Dolan ME. Genetic and modifiable risk factors contributing to cisplatin-induced toxicities. *Clin Cancer Res* 2019;**25**:1147−55.
29. Ding KK, Wang LR, Zhu JM, He D, Huang YH, Zhang WJ, et al. Photo-enhanced chemotherapy performance in bladder cancer treatment *via* albumin coated AIE aggregates. *ACS Nano* 2022;**16**:7535−46.
30. Wen XD, Zhang R, Hu YX, Wu LY, Bai H, Song DF, et al. Controlled sequential *in situ* self-assembly and disassembly of a fluorogenic cisplatin prodrug for cancer theranostics. *Nat Commun* 2023;**14**:800.
31. Rottenberg S, Disler C, Perego P. The rediscovery of platinum-based cancer therapy. *Nat Rev Cancer* 2021;**21**:37−50.
32. Cook JA, Gius D, Wink DA, Krishna MC, Russo A, Mitchell JB. Oxidative stress, redox, and the tumor microenvironment. *Semin Radiat Oncol* 2004;**14**:259−66.
33. Chaiswing L, Oberley TD. Extracellular/microenvironmental redox state. *Antioxid Redox Signal* 2010;**13**:449−65.
34. Dong X, Brahma RK, Fang C, Yao SQ. Stimulus-responsive self-assembled prodrugs in cancer therapy. *Chem Sci* 2022;**13**:4239−69.
35. Bai XP, Ni J, Beretov J, Graham P, Li Y. Triple-negative breast cancer therapeutic resistance: where is the Achilles' heel?. *Cancer Lett* 2021;**497**:100−11.
36. Wang LH, Wu DC, Xu HX, You YZ. High DNA-binding affinity and gene-transfection efficacy of bioreducible cationic nanomicelles with a fluorinated core. *Angew Chem Int Ed Engl* 2016;**55**:755−9.
37. Zhang ZJ, Shen WW, Ling J, Yan Y, Hu JJ, Cheng YY. The fluorination effect of fluoroamphiphiles in cytosolic protein delivery. *Nat Commun* 2018;**9**:1377.
38. Sun WH, Chen LJ, Zhang YM, Wang JL. Synergistic effect of ozonation and ionizing radiation for PVA decomposition. *J Environ Sci (China)* 2015;**34**:63−7.
39. Wu QY, Yang ZW, Du Y, Ouyang WY, Wang WL. The promotions on radical formation and micropollutant degradation by the synergies between ozone and chemical reagents (synergistic ozonation): a review. *J Hazard Mater* 2021;**418**:126327.
40. Garoma T, Gurol MD. Degradation of tert-butyl alcohol in dilute aqueous solution by an O3/UV process. *Environ Sci Technol* 2004;**38**:5246−52.
41. Li QQ, Shi ZQ, Zhang F, Zeng WW, Zhu DW, Mei L. Symphony of nanomaterials and immunotherapy based on the cancer−immunity cycle. *Acta Pharm Sin B* 2022;**12**:107−34.
42. Arina A, Gutiontov SI, Weichselbaum RR. Radiotherapy and immunotherapy for cancer: from "systemic" to "multisite". *Clin Cancer Res* 2020;**26**:2777−82.
43. Ma S, Song WT, Xu YD, Si XH, Lv SX, Zhang Y, et al. Rationally designed polymer conjugate for tumor-specific amplification of oxidative stress and boosting antitumor immunity. *Nano Lett* 2020;**20**:2514−21.
44. Monteran L, Ershaid N, Doron H, Zait Y, Ye Scharff, Ben-Yosef S, et al. Chemotherapy-induced complement signaling modulates immunosuppression and metastatic relapse in breast cancer. *Nat Commun* 2022;**13**:5797.
45. Kroemer G, Galluzzi L, Kepp O, Zitvogel L. Immunogenic cell death in cancer therapy. *Annu Rev Immunol* 2013;**31**:51−72.

46. Hato SV, Khong A, de Vries IJM, Lesterhuis WJ. Molecular pathways: the immunogenic effects of platinum-based chemotherapeutics. *Clin Cancer Res* 2014;**20**:2831−7.
47. Martins I, Kepp O, Schlemmer F, Adjemian S, Tailler M, Shen S, et al. Restoration of the immunogenicity of cisplatin-induced cancer cell death by endoplasmic reticulum stress. *Oncogene* 2011;**30**:1147−58.
48. Wu JC, Wang X, Chen L, Wang JN, Zhang JL, Tang JH, et al. Oxygen microcapsules improve immune checkpoint blockade by ameliorating hypoxia condition in pancreatic ductal adenocarcinoma. *Bioact Mater* 2023;**20**:259−70.
49. Yang ZB, Luo Y, Yu HZ, Liang KC, Wang M, Wang QG, et al. Reshaping tumor immune microenvironment based on light activated nano-platform for efficient cancer therapy. *Adv Mater* 2022;**34**:2108908.
50. Wu PK, Zhang HT, Sun ML, Mao S, He QF, Shi YZ, et al. Manipulating offense and defense signaling to fight cold tumors with carrier-free nanoassembly of fluorinated prodrug and siRNA. *Adv Mater* 2022;**34**:2203019.
51. Li GT, Sun BJ, Li YQ, Luo C, He ZG, Sun J. Small-molecule prodrug nanoassemblies: an emerging nanoplatform for anticancer drug delivery. *Small* 2021;**17**:2101460.
52. Li HN, Zang WL, Mi Z, Li JY, Wang LJ, Xie D, et al. Tailoring carrier-free nanocombo of small-molecule prodrug for combinational cancer therapy. *J Control Release* 2022;**352**:256−75.
53. Han H-H, Wang H-M, Jangili P, Li M, Wu L, Zang Y, et al. The design of small-molecule prodrugs and activatable phototherapeutics for cancer therapy. *Chem Soc Rev* 2023;**52**:879−920.